# Defective callosal termination underlies the long-term behavioral deficits in NMDA receptor antibody encephalitis mouse model

Jing Zhou[1,2,3*], Ariele L. Greenfield[1,2□], Rita Loudermilk[1,2□], Christopher M. Bartley[2,3,4□], Baouyen T. Tran[1,2,3], Chao Zhao[5], Hong Wang[1,2], Michael R. Wilson[1,2,3], Samuel J. Pleasure[1,2,3,6*]

□ equal contributions; *, corresponding authors

1. Department of Neurology, University of California, San Francisco, San Francisco, CA 94143, USA.
2. Weill Institute for Neurosciences, University of California, San Francisco, San Francisco, CA 94143, USA.
3. Center for Encephalitis and Meningitis, University of California, San Francisco, San Francisco, CA 94143, USA.
4. Department of Psychiatry, University of California, San Francisco, San Francisco, CA 94143, USA.
5. Center for Data Driven Discovery in Biomedicine, Children's Hospital of Philadelphia, Philadelphia, Pennsylvania, PA 19146, USA.
6. Programs in Neuroscience and Developmental Stem Cell Biology, Eli and Edythe Broad Center of Regeneration Medicine and Stem Cell Research, Kavli Institute for Fundamental Neuroscience, San Francisco, CA 94143, USA.

Electronic address: samuel.pleasure@ucsf.edu; jing.zhou@ucsf.edu

## Abstract

NMDA receptor antibody encephalitis (NMDAR-AE) is characterized by cerebrospinal fluid (CSF)-resident anti-NMDA receptor autoantibodies that cause a wide range of neurological manifestations. Although many symptoms are responsive to immunotherapy, behavioral deficits persist, especially in young patients. However, the underlying mechanisms of these long-lasting impairments are unknown. Here, we used a patient-derived GluN1 -specific monoclonal antibody (mAb) to interrogate the underlying mechanisms of long-lasting sensory-motor impairments. Transient exposure to this mAb led to excess callosal projections in somatosensory cortex and resulted in permanent callosal axon alterations in mice. Importantly, these mice displayed persistent fine movement impairments which were similar to those in NMDAR-AE patients. Notably, the severity of these behavioral deficits was tightly correlated with the severity of callosal axon alterations. At the injection site, the anti-GluN1 autoantibody significantly decreased EPH receptor B2 (EPHB2) expression, a regulator of commissural projections, indicating EPHB2's essential role in this phenotype. Our studies reveal important insights into the cellular and molecular basis for persistent sensory-motor deficits in NMDAR-AE.

## Introduction

NMDAR-AE is the most common form of autoimmune encephalitis, typically associated with antibodies against the extracellular domain of the GluN1 subunit of the NMDA receptor (NMDAR), and occurs most often in children and young adults (Dalmau et al., 2011; Dalmau et al., 2007). The most common symptoms of

NMDAR-AE include abnormal behavior, psychiatric symptomatology, memory impairment, movement disorders and seizures. Age-dependent variations in severity of the clinical manifestations were reported (Baizabal-Carvallo et al., 2013; Florance et al., 2009; Goldberg et al., 2014; Hacohen et al., 2014b).

Clinically, children represent more than one-third of reported cases of NMDAR-AE (Titulaer et al., 2013; Yeh, 2014), and suffer worse long-term behavior deficits than patients in adolescence or young adulthood (Gordon-Lipkin et al., 2017; Yeshokumar et al., 2022). Movement disorders are the most common persistent behavioral deficits in children (Duan et al., 2016; Varley et al., 2019). Earlier disease onset and longer treatment delays (> 4 weeks) are associated with a more severe disease course in children, including a higher risk of persistent sensory-motor deficits (Bartels et al., 2020). Animal studies have also shown that transplacental transfer of anti-NMDAR antibodies result in behavioral alterations in offspring (Garcia-Serra et al., 2021; Joubert et al., 2020; Jurek et al., 2019). Previous studies showed that anti-NMDAR antibody induced loss of axonal surface NMDAR and synaptic localization are reversible after immunotherapy and plasma exchange (Hughes et al., 2010; Kayser and Dalmau, 2011), but that neurological deficits persist in many patients (Titulaer et al., 2013). These observations from both clinical and basic research indicate that early exposure to anti-NMDAR autoantibodies may interfere with neurodevelopment, and the resulted persistent circuit impairments may lead to the long-term behavior deficits. Therefore, instead of injecting patient cerebrospinal fluid (CSF) into adult mice as previous studies reported (Planaguma et al., 2015; Wurdemann et al., 2016), in this study, we start the autoantibody exposure from postnatal day 3 (P3) to P12 in mice (equivalent to 1-5 year old in human).

The corpus callosum (CC) projects between somatosensory cortices and integrates sensory-motor information in order to control fine motor movements such as hand/finger dexterity (Iwamura, 2000; Iwamura et al., 2001). The CC is the largest white matter structure in mammals, and interhemispheric CC connectivity is essential for bilateral coordination and higher cognitive processes (Paul, 2011). In humans, the general shape of the CC is present at birth, but the CC continues to develop dynamically throughout childhood and into adolescence (Edwards et al., 2014; Hengst et al., 2010; Semple et al., 2013). Lesions in or volume loss of CC have been reported in NMDAR-AE patients (Du et al., 2020; Jan and Anilkumar, 2021; Wang et al., 2020), and the extent of white matter damage in NMDAR-AE patients correlates with disease severity (Finke et al., 2013; Hacohen et al., 2014a; Peer et al., 2017). Our previous study showed that genetic disruption of NMDAR led to defects of callosal projections in primary somatosensory cortex (S1) in mice, demonstrating NMDAR signaling regulates CC development (Zhou et al., 2021). This suggests that the CC may be particularly vulnerable to insult and could explain persistent sensory-motor deficits in children with NMDAR-AE.

Persistent behavioral deficits are common in a wide range of autoimmune neurological disorders including NMDAR-AE (Dalmau and Graus, 2018; Lancaster, 2016), but how autoantibodies cause these long-lasting sensory-motor deficits is largely unknown.

Here, we generated anti-GluN1 human monoclonal antibody (mAb) from CSF B-cells isolated from a patient with recurrent NMDAR-AE. We then used a novel model system to investigate the long-term consequences of transient mAb exposure on axonal morphology and callosal circuity, and correlated these structural changes with sensory-motor impairments.

## Results

### Generation and validation of patient-derived monoclonal anti-NMDAR antibodies

We isolated single, antigen-experienced B-cells from the CSF of a patient with NMDAR-AE using a piezoacoustic liquid handling device (Cellenion, Lyon, France and SCIENION, Berlin, Germany). After RNA extraction and RT-PCR of the heavy and light chains of the immunoglobulin genes of individual cells, we Sanger sequenced the amplicons and produced four distinct patient-derived human IgG1 mAbs using published approaches (Ramberger et al., 2020; Tiller et al., 2008a) (**Figure 1A**).

Immunoprecipitation (IP) with adult mouse brain lysate showed that patient CSF IgG and two of these mAbs (mAb1 and mAb3) bound NMDAR complexes (**Figure 1B**). Comparing with the negative control (**Figure 1C**), immunostaining of mouse brain tissue with patient CSF IgG, mAb1, and mAb3 produced intense, characteristic NMDAR neuropil staining in the hippocampus (**Figures 1D-1F**) (Dalmau et al., 2007; Jones et al., 2019; Moscato et al., 2014). Immunostaining live murine hippocampal neurons with mAb1 and mAb3 from *Emx1*$^{cre/+}$; *Grin1*$^{wt/wt}$; *Rosa26*$^{fs\text{-}tdTomato}$ mice, produced punctate cell-surface staining, where red fluorescence marks Cre-mediated recombination without deletion of NMDAR (**Figures 1G**, **1H**). The punctate cell-surface staining was lost in red cells of *Emx1*$^{cre/+}$; *Grin1*$^{fl/fl}$; *Rosa26*$^{fs\text{-}tdTomato}$ cultures (**Figure 1I**), which mark the individual NMDAR knock-out (KO) neurons with red fluorescent protein tdTomato, indicating that mAb1 and mAb3 directly bind NMDAR and recognize extracellular epitopes of NMDAR. This was consistent with previous reports that anti-NMDAR autoantibodies from NMDAR-AE patients recognize extracellular domain of NMDAR (Castillo-Gomez et al., 2017; Gleichman et al., 2012).

mAb1 and mAb3 share many of the common features of NMDAR staining. However, mAb3 presents a more uniform pattern (**Figure 1F**), while mAb1 stains stronger in the olfactory bulb, cortex, and hippocampus (**Figure 1E**). Also, mAb3 staining was seen prominently in neuronal cell bodies and processes, whereas mAb1 lacked this pattern (**Figure 1J**). Lastly, mAb1 staining was less prominent than mAb3 staining in postnatal day (P) 8 mouse brain (**Figure 1-figure supplementary 1**). These overlapping but different spatial and temporal staining patterns suggested that mAb1 and mAb3 may recognize different subunits of NMDAR.

### mAb3 binds the GluN1 subunit, while mAb1 binds the GluN2A subunit

NMDARs are heteromeric receptor Ca$^{++}$ channel complexes with various subunit compositions. To date, seven different subunits have been identified: the GluN1 subunit, four distinct GluN2 subunits (A-D), and two GluN3 subunits. The GluN1 subunit is required for all functional NMDARs (Dingledine et al., 1999; Paoletti et al., 2013). In the forebrain, GluN1 primarily assembles with GluN2A and GluN2B to form functional NMDARs. GluN2A- and GluN2B-containing NMDARs follow different developmental expression trajectories with GluN2B as the major NR2 subunit during the first postnatal week, and GluN2A expression beginning in the first postnatal week and increasing thereafter to become the dominant NR2 subunit in adults (Liu et al., 2004; Monyer et al., 1994; Sans et al., 2000; Sheng et al., 1994). Because of the uniform staining pattern of mAb3 during development and in adulthood (**Figure 1-figure supplementary 1 and Figures 1F**), we hypothesized that mAb3 may recognize the GluN1 subunit. The weak staining of mAb1 during development (**Figure 1-figure supplementary 1**) with strong staining in adulthood (**Figure 1E**), as well as its distinct staining pattern in the forebrain (**Figure 1E**), suggested that mAb1 may recognize the GluN2A subunit.

To determine the subunit specificity of mAb1 and mAb3, we evaluated staining patterns in GluN1 KO, GluN2A KO, and GluN2B KO mice. In *Emx1*$^{cre/+}$; *Grin1*$^{fl/fl}$; *Rosa26*$^{fs\text{-}tdTomato}$ mice, the GluN1 subunit was knocked out and all NMDARs failed to assemble in red cells. Consistent with our results shown in **Figure 1**, in brain sections from control *Emx1*$^{cre/+}$; *Grin1*$^{wt/wt}$; *Rosa26*$^{fs\text{-}tdTomato}$ mice, mAb1 staining was mostly present in neuropil but less on cell bodies; while mAb3 staining was both detected in neuropil and on cell bodies (**Figure 2Bi**). However, the punctate staining of mAb1 was dramatically decreased in brain sections of *Emx1*$^{cre/+}$; *Grin1*$^{fl/fl}$; *Rosa26*$^{fs\text{-}tdTomato}$ mice (**Figures 2Bii, 2C and 2D**) and somatic staining of mAb3 was completely lost in red (recombined) cells of *Emx1*$^{cre/+}$; *Grin1*$^{fl/fl}$; *Rosa26*$^{fs\text{-}tdTomato}$ brain sections (**Figures 2Bii and 2E**), further confirming that the two mAbs directly bind NMDAR. Next, we examined their staining pattern in *Emx1*$^{cre/+}$; *Grin2a*$^{fl/fl}$ mice, lacking GluN2A-containing NMDARs in excitatory cortical neurons. Compared with brain sections of control *Grin2a*$^{fl/fl}$ mice, the punctate fiber staining of mAb1 in *Emx1*$^{cre/+}$; *Grin2a*$^{fl/fl}$ mice was significantly decreased (**Figures 2Fi, 2Fii and 2G**, $P<0.0001$). However, there was no difference of mAb3 staining between these mice (**Figures 2Fi, 2Fii and 2H**). These results suggested that mAb1, but not mAb3, directly binds to the GluN2A subunit of NMDAR. Then, we examined their staining pattern in *Emx1*$^{cre/+}$; *Grin2b*$^{fl/fl}$; *Rosa26*$^{fs\text{-}tdTomato}$ mice, in which GluN2B-containing NMDARs were deleted in red cells. There was no difference in the staining for either mAb1 or mAb3 in brain sections of *Emx1*$^{cre/+}$; *Grin2b*$^{fl/fl}$; *Rosa26*$^{fs\text{-}tdTomato}$ and control *Emx1*$^{cre/+}$; *Grin2b*$^{wt/wt}$; *Rosa26*$^{fs\text{-}tdTomato}$ mice (**Figures 2I-2K**). This result suggests that neither of the two mAbs binds to the GluN2B subunit of NMDAR. Since mAb3 did not directly bind to either GluN2A or GluN2B subunits, but bound to NMDAR, mAb3 must bind directly to the GluN1 subunit of NMDAR. Taken together, these results suggested that mAb3 binds the GluN1 subunit, while mAb1 binds the GluN2A subunit. According to Kreye et al. (2016) (Kreye et al., 2016), autoantibodies targeting the GluN1 subunit of NMDAR are believed to be the main autoantibodies responsible for NMDAR-AE. Therefore, in this study, we utilized mAb3$^{[GluN1]}$ to investigate the underlying mechanisms behind persistent sensory-motor deficits in a mouse model.

### mAb3$^{[GluN1]}$ injection disrupts callosal projection patterns in primary somatosensory cortex

The callosal projection pattern of primary somatosensory cortex (S1) in mice reveals initial diffuse projections to S1 at P8, with refinement of the innervation at the primary somatosensory cortex/secondary somatosensory cortex (S1/S2) border at P14. We previously demonstrated that NMDAR in the target S1 controls the pattern and terminal density of afferent callosal axonal projections (Zhou et al., 2021) by showing that genetic and commercial antibody-mediated loss of function of NMDAR in contralateral target S1 but not in ipsilateral projecting S1 causes diffuse and more overall callosal axons innervating S1 at P14. This phenotype is not mediated by the ion channel function of NMDAR but instead mostly depends on the interactions between NMDAR and the axon guidance signaling pathway EPHRIN-B/EPHB.

To test whether exposure to human pathogenic anti-NMDAR autoantibodies disrupts commissural S1 circuit formation, we injected the mAb3$^{[GluN1]}$ into mice during callosal development. We first labelled layer II/III callosal neurons by *in utero* electroporation of progenitor cells with enhanced green fluorescent protein (EGFP) at embryonic day (E) 15.5 (**Figure 3A**). Then we injected mAb3$^{[GluN1]}$ (1.6μg) into the contralateral target S1, twice-daily from P3 to P12, and examined the callosal projection pattern at P14 (**Figures 3B-3D**). The feasibility and efficiency of this cortical antibody injection (**Figure 3-figure supplementary 1**) was demonstrated in our previous study (Zhou et al., 2021). Injection of mAb3$^{[GluN1]}$ led to a diffuse projection pattern and significant increase in the callosal projections in contralateral S1 at P14 relative to control human IgG (1.6 μg, Jackson ImmunoResearch) (**Figure 3C and 3D**, $P < 0.0001$) , which is consistent with our genetic data showing that *Grin1* loss-of-function increased callosal projections in S1 (Zhou et al., 2021).

We next used quantitative immunofluorescence to determine whether, like genetic NMDAR disruption, patient-derived mAb downregulate the EPHRIN/EPH pathway, which is essential for callosal projection (Zhou et al., 2021). We found that the expression of EPHB2 was dramatically reduced in mAb3$^{[GluN1]}$-treated S1 (**Figures 3E-3G**), indicating EPHB2 participated in impaired callosal projections induced by mAb3$^{[GluN1]}$. This is consistent with genetic data (Zhou et al., 2021), but also with a previous study which indicated that EPHB2 interacts with NMDAR via GluN1 (Dalva et al., 2000; Nolt et al., 2011; Planaguma et al., 2016).

### Permanent alterations of S1 callosal axons in mice exposed transiently to mAb3$^{[GluN1]}$ during development

To determine if the early, transient exposure to antibodies resulting in callosal circuit disruption last to adulthood, we anatomically examined the S1 callosal circuit at P120. Interestingly, by P120, the excess S1 callosal projections seen in mice treated with mAbs during development had resolved (**Figures 4A and 4B**). However, we also assessed cell morphology at the single-cell level by tracing individual callosal axon terminals in S1 (**Figures 4C, Figure 4-figure supplementary 1**, **Materials and methods**) and assessing morphometric features, including terminal field areas, numbers of branch points and terminal points, total branch length, branch diameter, branch resistance, branch levels, branch angles, and branch orientations.

Unexpectedly, axon terminal morphology in S1 was permanently altered in mAb3$^{[GluN1]}$-treated mice in a sex-specific manner months after the transient exposure to antibody (**Table 1**). mAb3$^{[GluN1]}$-treated males displayed significantly higher numbers of axon branch crossings using Sholl analysis (**Figures 4D**), suggesting increased branch complexity and larger terminal field areas (Bird and Cuntz, 2019). mAb3$^{[GluN1]}$-treated female and male mice displayed significantly increased axon branch points, terminal points, and total branch length (**Figures 4E, 4F**), consistent with higher branch complexity. Importantly, mAb3$^{[GluN1]}$-treated male mice also displayed significantly reduced branch diameter (**Figure 4F**), suggesting increased axon resistance (**Figure 4F**) which may decrease conduction velocity in signal propagation. In addition, mAb3$^{[GluN1]}$ male mice displayed significantly increased axon branch levels (**Figure 5F**), branch angles (**Figure 4-figure supplementary 2**) and altered branch orientation angles (**Figures 4H**). As shown in **Figure 4C**, most axon branches should be directed toward the pia at the cortical surface. However, many axons in mAb3$^{[GluN1]}$ male mice branched away from the cortical surface, leading to reduced branch orientation angle (**Figures 4H**).

### Persistent sensory-motor deficits in mice treated with mAb3$^{[GluN1]}$ during development

Callosal projection in S1 is essential for bilateral sensory-motor integration (**Figure 4-figure supplementary 3A**). The callosal axon terminals in S1 are the key structures to propagate and coordinate bilateral sensory signal conduction. The S1 callosal terminal defects in mAb3$^{[GluN1]}$-treated mice included reduced axon diameter, increased branch complexity, and altered geometry in axon terminals (**Table 1**). These malformations may interfere with the sensory processing and sensory-motor integration (Alcami and El Hady, 2019) (**Figure 4-figure supplementary 3B**). Thus, we wondered whether these persistent morphological alterations could cause lasting sensory-motor deficits.

Thus, we performed a battery of behavioral tests in mice from 1- to 4-months-old. To assess overall motor activity levels, we measured baseline anxiety using an elevated plus maze (EPM), and baseline locomotor activity with the repeated open field test (OFT). Time spent in the open arms of EPM (**Figure 5-figure supplementary 1**), which measures anxiety-like behavior, along with distance traveled in the EPM (**Figure 5-figure supplementary 1**), were similar between the groups. Total movements in the OFT (**Figures 5A and 5B**), which measures locomotor activity, were also similar between groups. These observations indicated that mAb3$^{[GluN1]}$-treated animals and controls had similar levels of anxiety and overall locomotor activity.

Next, we performed a battery of more specific sensory-motor tasks. In measures of coarse movement function, - burrowing test (**Figures 5C and 5D**) (measuring digging and kicking activity) and rotarod (**Figures 5E and 5F**) (measuring sensory-motor coordination), mice showed comparable performance between the groups.

In contrast, mAb3$^{[GluN1]}$-treated mice showed significant impairments in fine motor tasks, including nest building (Jirkof, 2014), balance beam and the facing upward pole test (**Figures 6, Video S1-S8**). Generally, in tasks involving fine motor skills and sensory integration, we observed a sex difference: male mice treated with mAb3$^{[GluN1]}$ showed more severe impairment than female mice treated with mAb3$^{[GluN1]}$ (**Table 2**).

Specifically, mAb3$^{[GluN1]}$-treated male mice showed significantly impaired nest building (**Figure 6B**); mAb3$^{[GluN1]}$-treated female (**Figures 6D, Video S2**) showed significantly increased balance check in the initial training Trail to cross the small beam; mAb3$^{[GluN1]}$-treated female mice (**Figures 7L, Video S6**) showed significantly extended descending time during the earlier training phase of the facing upward pole test, while mAb3$^{[GluN1]}$-treated male mice (**Figure 7M, Video S8**) showed significantly extended descending time during the later testing phase of the facing upward pole test. There was no correlation between motor performance and body weight, muscular strength, or coordination (**Figure 6-figure supplementary 1 - 4**). These results demonstrate that transient exposure to pathogenic anti-NMDAR autoantibodies results in persistent fine sensory-motor deficits in mice. Most interestingly, the morphological alterations of S1 callosal axons were highly and positively correlated with the behavioral deficits in sensory-motor coordination. mAb3$^{[GluN1]}$-treated male mice with most altered morphology in S1 callosal terminals displayed the worst behavioral performance in sensory-motor coordination (**Tables 1 and 2**), suggesting that callosal termination defects underlies the long-term sensory-motor deficits in NMDAR-AE.

## Discussion

Important advances have been made in understanding the pathophysiology of NMDAR-AE during the acute phase (Dalmau, 2016). However, despite initial responsiveness to immunotherapy, these patients are often left with residual cognitive deficits and behavioral abnormalities, even after the autoantibody titers have decreased (Gresa-Arribas et al., 2014). The basis of these persistent impairments is not well-understood. Here, we showed in a mouse model that transient exposure to patient-derived anti-NMDAR autoantibodies resulted in long-lasting deficits in fine sensory-motor tasks. Taking full advantage of electroporation, for the first time, we demonstrated that the defective callosal termination to somatosensory cortex plays an essential role in the pathogenesis of behavior deficits induced by NMDAR autoantibodies. Our study models what may be the cellular basis of the protracted sensory-motor deficits observed in NMDAR-AE patients.

We have demonstrated that callosal circuit formation in the mouse is most sensitive to anti-NMDAR antibodies between P6 and P8 (Zhou et al., 2021), which is equivalent to a 2–3-year-old child. A brain MRI study in a cohort of pediatric NMDAR-AE patients found earlier age of first exposure to the antibodies and longer treatment delays (> 4 weeks) are associated with a more severe disease course in children. A child of 2-year-old at disease onset showed progressive brain volume loss and persistent deficits after a two-year follow-up, whereas an 11-year-old child showed reversible brain volume loss correlating with full recovery (Bartels et al., 2020). Interestingly, volume loss of the CC was observed in another 2-year-old child with delayed diagnosis of NMDAR-AE, who presented with severe symptoms and persistent neurological impairment (Jan and Anilkumar, 2021). The persistent deficits in these 2-year-old patients are aligned to the previous findings that the extent of white matter damage in NMDAR-AE patients is correlated with disease severity (Finke et al., 2013; Hacohen et al., 2014a; Peer et al., 2017). These clinical observations suggest the possible involvement of the CC in brain network alterations in NMDAR-AE and support our experimental conclusions that developmental exposure to anti-NMDAR antibodies can cause persistent circuit deficits even long after definitive treatment leading to diminished autoantibody levels.

Coordination of the hands and fingers relies on communication through the CC in somatosensory cortex (Iwamura, 2000; Iwamura et al., 2001). Each subcortical neuron in somatosensory cortex responds to specific stimuli applied to a specific region of the body. The sensory information sampled by two halves of a body is integrated bilaterally at the cortical level via the CC. As shown in our mouse models, it is possible that the axon morphology of S1 callosal neurons are irreversible altered in young children exposed to anti-NMDAR autoantibodies during critical time window of CC development. The S1 callosal terminals with higher branch complexity, increased axon resistance and altered branch orientation angles (**Figures 4 and Figure 4-figure supplementary 2**), could slow bilateral signal propagation (Alcami and El Hady, 2019), thus disrupt sensory-motor integration, and lead to persistent sensory-motor deficits in children (Bartels et al., 2020).

Autoantibodies targeting the GluN1 subunit of NMDAR are believed to be the main pathogenic autoantibodies in NMDAR-AE (Kreye et al., 2016). In line with this finding, we isolated the anti-GluN1 mAb (mAb3) from a patient with NMDAR-AE. However, we also identified the presence of anti-GluN2A mAb (mAb1) in this patient, which is a novel finding not previously reported in NMDAR-AE patients. Further characterization is required to understand the nature of this novel autoantibody.

In this study, we characterized monoclonal anti-GluN1 autoantibody from a NMDAR-AE patient and made use of it to generate mice with sensory-motor deficits similar to those in pediatric patients. We discovered that callosal termination to somatosensory cortex was disrupted in these mice. The expression of EPHB2, a known regulator of callosal projection, also decreased in somatosensory cortex. In addition, both callosal defects and sensory-motor deficits varied by sex, and analysis of these differences showed that disrupted callosal terminations in S1 were associated with the degree of sensory-motor impairment. This finding is consistent with S1's known role in somatosensory integration. These results demonstrate that transient developmental exposure to patient-derived NMDAR autoantibodies result in persistent alterations in callosal axon morphologies and callosal circuit disruption, thereby providing a basis for enduring sensory-motor deficits in convalescent pediatric NMDAR-AE patients.

## Materials and methods

### Experimental Model and Subject Details

All animal protocols were in accordance with the regulations of the National Institute of Health and approved by the University of California San Francisco Institutional Animal Care and Use Committee (IACUC). Floxed NR1 allele (Stock #005246), EMX1-Cre (Stock #005628) and Ai14 Cre reporter allele (Stock # 007914) were obtained from Jackson Laboratories (Bar Harbor, ME, USA). Floxed *Grin2a* and *Grin2b* alleles were provided by the laboratory of Prof. Roger Nicoll. Wild-type CD1 mice were obtained from Charles River Laboratories. Male and female embryos at embryonic (E) 15.5 were used for the *in utero* electroporation, and pups between postnatal day 0 (P0) to 14 (P14) for the experiments.

***In utero* Electroporation:** DNA solution including the plasmid and 0.04% fast green was injected into the medial region of the lateral ventricle of the embryonic brain with a glass micropipette. Electrical pulses then were delivered to embryos by electrodes connected to a square-pulse generator (ECM830, BTX). For each electroporation, five 35-V pulses of 50ms were applied at 1s intervals. After the electroporation, the uterus was returned to the abdominal cavity, followed by suturing of the abdominal wall and skin. Mice were perfused at different postnatal stages using 4% paraformaldehyde followed by post-fixed overnight and incubation in 30% sucrose at 4°C. 35 μm-thick coronal sections were obtained using cryostat sectioning.

**Plasmid:** The ubiquitin-EGFP plasmid used was from a previous study (Zhou et al., 2013).

**Antibodies: Antibodies for intraventricular injection**: Patient derived monoclonal anti-NMDAR antibodies were made by Ariele Greenfield and Rita Loudermilk in Michael Wilson's lab (For details see **Methods for making monoclonal antibody from anti-NMDAR encephalitis patient**). Human IgG (#009-000-003, Jackson ImmunoResearch) served as control. **Antibodies for immunostaining**: goat anti-EphB2 (1:50, AF467, R&D), anti-human 488 (#109-545-088, Jackson ImmunoResearch), donkey anti-goat cy3 (#705-165-003, Jackson ImmunoResearch). **Antibodies for immunoprecipitation:** human IgG (#009-000-003, Jackson ImmunoResearch), CSF from patient without anti-NMDAR encephalitis patient (neuropsychiatric lupus), CSF of anti-NMDAR encephalitis patient, monoclonal antibodies (18-20ug/ml for immunostaining) mAb1, mAb2, mAb3, mAb4 made from the anti-NMDAR encephalitis patient. **Antibodies for western blot**: rabbit anti-NR1 (AB9864, Millipore), IRDye 800CW Goat x Rabbit IgG(H+L) Ab (1:20000, #925-32211, Li-Cor).

### Methods for Making Monoclonal Antibody from anti-NMDAR Encephalitis Patient

#### *Patient Recruitment and Eligibility Criteria*

Inclusion criteria for this study was enrollment in "Immunological Studies in Multiple Sclerosis, Neuromyelitis optica, Sarcoidosis, or Immune Mediated Central Nervous System Disorders" and diagnosis of antibody-positive NMDA receptor encephalitis. The patient is a 21-year-old Hispanic male who was experiencing his second attack of anti-NMDAR encephalitis. His first attack was treated with steroids and IVIg and he was then able to stop immunotherapies. Three years later, he became encephalopathic for a second time, and was again found to have detectable anti-NMDAR antibodies in the CSF. The patient consented to donating CSF and blood, and patient demographics and clinical history were obtained as part of the above study. All studies were approved by the UCSF Institutional Review Board.

*Patient Cerebrospinal Fluid Collection, Processing and Fluorescence-activated cell sorting (FACS)*

12 ml of fresh CSF was centrifuged at 400g x 15 minutes at 4°C to separate a cell pellet from supernatant. Supernatant was removed immediately to avoid cell dispersion, and care was taken to minimally move the source 15ml conical tube. Wide bore pipette tips were used when handling cells to preserve cell integrity.

Destination FACS tubes (1.5ml Eppendorf) were coated overnight with 100% FBS to minimize cell adhesion. Destination tubes were filled with 450μl of cold D-PBS + 15% FBS and placed lid-open in front of a de-static bar prior to placing them in the cell sorter. Cell samples were blocked with FcR Block (Miltenyi Biotec) and stained with fluorescent antibodies to cell surface markers: IgD Brilliant Violet 421 (Biolegend 11-26c.2a), CD20 FITC (Beckman Coulter B9E9), CD38 PerCPCy5.5 (BioLegend HIT2), CD3 PE-Cy7 (Beckman UCHT1), CD138 PE (Miltenyi 449), CD27 APC (eBioscience O323), CD19 APC-Alexa750 (Beckman J3-119). CSF B cell subsets were sorted on a Beckman MoFlo Astrios FACS sorter as previously described (Eggers et al., 2017). CD27hi plasmablast/plasma cells (CD27hiPC: CD19+IgD-CD27hi), the vast majority of which are also CD38+, were then used for single cell printing.

*Single Cell Printing of FACS-sorted CSF cells*

CD27$^{hi}$PC cell suspensions were diluted to a 5% FBS concentration immediately prior to being centrifuged at 300g x 5min at 4°C. Pelleted cells were gently resuspended in 5-20μl of supernatant then placed on ice in a vacuum chamber for 5min. A ~5μl droplet of cells was pipetted onto a hydrophobic slide and aspirated for single cell printing by the CellenONE/sciDROP PICO system (Cellenion, Lyon, France and SCIENION, Berlin, Germany). Single cells were detected by the CellenONE and dispensed into wells of a 384-well PCR plate filled with 2μl/well of lysis buffer as described in the Smart-seq2 protocol (Picelli et al., 2014).

*Single cell immune repertoire sequencing and monoclonal antibody production*

Cell-containing PCR plates were briefly vortexed and centrifuged at 2000 rpm x 1 minute, placed on dry ice and immediately stored at -80°C. We then performed RT-PCR using template switching and total cDNA amplification and bead clean as previously described (Picelli et al., 2014). This was followed by targeted PCR of the heavy and light chains using primers to the leader sequences and constant region 1, followed by nested PCR as previously described (Tiller et al., 2008b). Products were sequenced via Sanger sequencing. Mapping of germline V, D, J and CDR3 regions was performed using IgBlast and IMGT V-Quest. Alignments were generated in Geneious (Biomatters). Recombinant monoclonal antibodies were produced with a high throughput method using a mammalian cell line (Tuna293) at LakePharma (San Carlos, CA), with mass spectrometry validation that the monoclonal antibody amino acid sequence matched the patient-derived Sanger sequence.

**Hippocampal Neuronal Cultures**: Hippocampi from male and female *Emx1*$^{cre/+}$; *Grin1*$^{fl/fl}$; *Ai14*$^{fl/fl}$ and littermate *Emx1*$^{cre/+}$; *Grin1*$^{wt/wt}$; *Ai14*$^{fl/fl}$ mice were dissected at P0-P1 and incubated with trypsin at 37° C for 15 min. Cells were then dissociated by trituration with fire-polished Pasteur pipettes. Neurons were plated on poly-D-lysine (Sigma-Aldrich) and mouse laminin (Invitrogen) coated 12 mm glass coverslips (Warner Instruments) at $5x10^4$ cells per well in a 24-well plate in plating media (minimal essential medium [MEM], 10% FBS, 0.5% glucose, 1 mM sodium pyruvate, 25 µM glutamine, and 50 units penicillin/streptomycin). After 4 h, medium was changed to Neurobasal medium supplemented with B-27 (Gibco), GlutaMAX (Gibco), and 50 units pen/strep (Gibco). Cultures were maintained in an incubator with 5% CO2 at 37°C, and half of the medium was replaced as needed.

**Live Neuron Staining**: At DIV 21, neurons were incubated with in-house monoclonal antibodies for 2 hours at 37°C. Following incubation, neurons were washed with warmed PBS and fixed with ice-cold 4% PFA in 0.1 M Na-acetate, pH 6.0 for 20 min at 4°C and washed thoroughly with PBS. Neuron-plated coverslips were blocked in 10% serum, 0.1% Triton-X-100 for 2 hours at room temperature. Primary antibodies were probed with donkey-anti-human Alexa Fluor 488 (Invitrogen) for 2 hours at room temperature and mounted in Prolong Gold (Invitrogen). Images were acquired using a Nikon Ti microscope equipped with an Andor Borealis CSU-W1 spinning disk confocal and Andor Zyla sCMOS camera (Nikon Core UCSF).

**Intraventricular Injection:** Antibodies were injected to lateral ventricular of pups by glass pipette with a sharp bevel at 45 degrees (BV-10 Micropipette Beveler, Sutter instrument). The diameter of pipette tip was ~40-80µm (Vogt et al., 2015). The concentrations for antibody injections were 2.0µg/µl for mAbs and Hum IgG. Antibodies were injected twice-daily, and the injection volume was 0.8-1µl for each injection.

**Methods to Prevent Bias**: Mouse pups delivered from one dam were randomly assigned for injection. Pups from different dams at the same time were grouped for experiment. Pups were raised by mother until postnatal 28 days. After weaning, mice with different treatments were mixed-housed. The investigator was blinded to group allocation and data analysis.

**Slice Preparation and Imaging:** Mice were perfused with saline followed by 4% paraformaldehyde in phosphate buffered saline (PBS), pH7.4. Brains were removed from mice and post-fixed in 4% paraformaldehyde overnight before being placed in 30% sucrose solution. The brains were then cut into 12-µm, 35-µm and 200-µm sections with cryostat (Leica VT1200S). Sections were imaged by Zeiss Axioscan Z.1

(Zeiss, Thornwood, NY, USA) with a 20X objective. Confocal images were taken by Zeiss LSM880 (Zeiss, Thornwood, NY, USA) with 20X objective, 63X oil objective and 100X oil objective.

**Immunostaining:** Mice were perfused with saline followed by 4% paraformaldehyde in phosphate buffered saline (PBS), pH7.4. Brains were removed from mice and post-fixed in 4% paraformaldehyde overnight before being placed in 30% sucrose solution. The brains were then cut into 12-μm sections with cryostat (Leica VT1200S). Non-specific binding was blocked by adding 5% normal goat/donkey serum during pre-incubation and incubations in 1x PBS containing 0.05% TritonX-100. The primary antibodies were applied overnight at 4 degrees. Secondary antibodies were applied for 1-2 hours at 4 degree and nuclei were stained with DAPI. Slides were mounted with Prolong Gold Anti-fade Mountant (P36930, Invitrogen).

**Immunoprecipitation (IP):** Adult mice at P40 were used for immunoprecipitation. **A single** mouse brain was homogenized in homogenizing buffer (1% Triton X-100, 150 mM NaCl, 50 mM Tris-HCl pH 7.5, 2 cOmplete protease inhibitor tablets (Roche), 1 phosSTOP phosphatase inhibitor tablet (Roche)) with Dounce homogenizer on ice. The lysate was then centrifuged at 10,000g for 10 min at 4°C. For each IP, 300μl of supernatant was transferred into a labelled IP tube and 700 μl of lysis buffer was added to achieve ~2 μg/ μl brain lysate. 30μg monoclonal antibody (mAb) or ChromoPure IgG control (Sigma) was added to each IP tube and mixed by rotator for 4hr at 4°C. Then, 50uL of equilibrated magnetic protein A/G beads (Thermo Scientific) were added to each IP reaction and mixed by rotator for 1hr at 4°C. Afterward, beads were washed with cold lysis buffer three times. At last, 50 μl sample buffer was added to beads to elute the protein and the IP elution was then subjected to western blotting by SDS-PAGE of IP eluates on a 4-12% Bis-Tris gel.

## Quantification and Statistical Analysis

**Callosal Axon Density Analysis**: Sections were imaged by Zeiss Axioscan Z.1 (Zeiss, Thornwood, NY, USA) with 20X objective over whole brain section. Each image was made up by the compression of three slices in 4μm Z-stack. For each brain, only one section was chosen for data quantification. The callosal axon density (fluorescence density) in S1 was quantitatively analyzed by ImageJ software. See the details in Zhou et al., (Zhou et al., 2021)

**Individual Axon Terminal Tracing**: 200-μm coronal section of P120 mouse brain were imaged by Zeiss LSM880 (Zeiss, Thornwood, NY, USA) with 20X objective. 3D confocal image of S1 callosal axon terminals loaded in Imaris 9.8 (Oxford Instruments). The morphology of individual callosal axon terminals was tracked manually with combining Autopath function in Imaris. All calculations on traced callosal axon terminals were automatically done by Imaris.

**Statistical Analysis:** Statistical analyses were performed with Prism 9 (GraphPad Software, San Diego, CA) and R version 4.1.0 with package such as ggplot2. Data are presented as scatterplots with mean ± standard error (SE). The statistical analyses used in this study included the student T-test, analysis of variance (ANOVA), Mann-Whitney test, Kruskal-Wallis test, and Dunn's multiple comparisons test. Each of these tests was listed in the legend of their respective figures. $p < 0.05$ was considered statistically significant.

### Mouse Behavioral Tests

All mouse behavioral tests were runed in Gladstone Behavioral Core. The use and care of the mice complied with the guidelines of the Institutional Animal Care and Use Committee of UCSF. All animals were maintained in 12 hr light/dark schedule and with access to food and water, ad libitum. Before behavioral testing, mice were transferred to the testing room and acclimated for at least 1 hour. All work surfaces were cleaned with Vimoba (100 ppm chlorine dioxide solution made from MB-10 Tablets, Quip Laboratories) before and after testing every day and with 70% alcohol between testing of different mice.

### Elevated Plus Maze Test

Elevated plus maze is used to evaluate anxiety-related behavior. The maze consists of two open and two enclosed arms elevated 63 cm above the ground (Hamilton-Kinder, Poway, CA). Mice are placed at the intersection between the open and closed arms and allowed to explore for 10 min. Anxiety-related behavior was measured by the time and distance traveled in the open arm.

### Open Field Test

Open field test is used to measure locomotion and anxiety-related behavior. Mice are placed in the center area of open field chamber (16 in x 16 in) with dim light in the dark phase for 10 min. Mice trajectory was recorded with photobeam assays (San Diego Instrument, San Diego, CA). Center area is an 8 in x eight in square in the center part of the chamber. Anxiety-related behavior was defined by ratio of traveled in the center area to total area. Total movements, rearing in the open field, and time spent in the center and periphery of the open field were recorded automatically for subsequent analysis.

### Nest Building Behavior Test

Nest building is spontaneous home cage behavior of mice. For assessment of nest building behavior, group-housed mice were transferred individually to new cages. A 5 × 5-cm white compressed cotton pad (Nestlets, Ancare) was placed in the center of the cage, and nest building behavior was assessed 2, 6, and 24 hours later. Composite nest building scores were assigned at each time point as follows: 0, nestlet untouched; 1, < 10% of nestlet shredded; 2, 10%–50% of nestlet shredded but nest was without shape; 3, 10%–50% of nestlet shredded and nest had shape; 4, 50%–90% of nestlet shredded but nest was without shape; 5, 50%–90% of nestlet shredded and nest had shape; 6, > 90% of nestlet shredded but nest was flat; and 7, > 90% of nestlet as shredded and nest had walls that were at least as tall as the mouse on > 50% of its sides.

### Burrowing Behavior Test

Burring behavior is used to evaluate spontaneous home cage behavior of mice. A burrow is made of 200 mm long, 68 mm diameter tube. The open end of the tube is raised 30 mm by bolting two 50 mm machine screws through it, each 10 mm in from the end. The lower end of the tube is closed with a plug. Fill the burrow with 200 g food pellets for mice and place the burrow against the longer wall of a clean cage with a thin layer of bedding. The closed end of the burrow is against the back wall of the cage. Provide water but no extra food in the cage hopper for the mice. Test is started 3hr before dark cycle. The displaced food pellets in the burrow were measured at 2hr and 24hr after cage-burrow setup.

### Rotarod Test

Rotarod is used to evaluate motor coordination of mice. Rotarod was performed with a Med Associates ENV-575(M) apparatus, using a 3-day protocol. Day 1 involved three training runs at fixed 16 rpm. Days 2 and 3 each involved 6 data runs, 3 in the morning and 3 in the afternoon. The data runs on days 2 and 3 used steady acceleration of the rod from 4-40 rpm over 5 min. The time was stopped at 5 min or when the mouse fell. Photobeams were interrupted by the experimenter if the mouse held onto the rod without walking for three full rotations. Each mouse was given three trials at least with a 15-min inter-trial interval and a maximum of 300 s per trial. The average latency to fall off the Rotarod was calculated.

### Balance Beam Test

Balance beam is used to evaluate motor coordination and balance. A 15” long plastic beam is suspended about 20” above the table, with an open platform at one end and a dark box with 1.5” square opening at the other end. Balance beam test was taken place over 3 days with 3 trials per day. The first day included two additional training trials. On the first training trial of the first day, mice were placed on the middle of the largest diameter beam facing a dark box and guided to the enclosure. On the second training trial on the first day, mice were placed on the end of the beam facing the dark box and guided to the enclosure. On the third to fifth trials (testing trials) on the first day, mice were placed on the end of the beam facing the dark box and traversed the beam unguided. On the second day, mice were placed at the end of the medium diameter beam, facing the dark box. On the third day, mice were placed at the end of the smallest diameter beam, facing the dark box. Latency to traverse the beam into the dark box, number of foot slips, and the number of falls were recorded. Trials were limited to a maximum latency of 60s.

### Pole Test

The pole test evaluates the ability of the mouse to grasp and maneuver on a pole in order to descend to its home cage. The vertical pole is 50 cm long (1 cm diameter) with rough surface. The base of the pole was placed in the home cage. Pole test was taken place over 2 days. The first day included three facing down training Trails and three facing up testing trials. The second day included three facing up testing Trails. In the training Trails, mice were placed facing down atop of the pole and the time to descend the pole was measured. In the testing Trails, mice were placed upward atop of the pole. The latency for mice to turn around and climb down was recorded. Any slips or falls in both training and testing Trails were also recorded. If a mouse falls at the beginning of the trial due to placement issues, mouse is replaced, and trial is restarted.

### Grip Strength Test

The Grip Strength test is a complement to behavioral tests for motor coordination and motor function. The Grip-Strength Meter (Ugo Basile) was used to measure the grip strength on forelimbs and all limbs. Mice were placed over a base plate, in front of a grasping bar (either trapeze-shaped or the grid), whose height is adjustable. The grasping tool is fitted to a force sensor connected to the Peak Amplifier, which guarantees a reliable and automated detection of the animal response. The force transducer has a maximum applicable force of 1500g, with a resolution 0.1g.

### Inverted Grid Hang Test

The inverted grid hang test is used to measure the ability of mice to exhibit sustained limb tension to oppose their gravitational force. The apparatus consists of a 15x25 cm grid of fine wire mesh suspended 34 cm above the table on supports. The walls and rear of the supports are covered with smooth plastic boards to prevent escape, and a larger plastic board is placed atop the wire mesh to prevent a mouse from climbing around the edge. The tabletop was covered with layers of soft towels to prevent injury from a fall. Mice were placed on the wire mesh, gently shaken to ensure a grip, and the mesh then inverted onto the supports. Latency to fall was recorded within 180 s. Measurements were repeated three times.

## Acknowledgements

We thank Jeffrey Simms in Gladstone Behavior Core for helping with experimental design and data analysis on behavior tests. We thank Dan Wang in Dr. Dena Dubal's lab at UCSF for helping with behavior tests and data analysis. We thank Qin Ma in Dr. Jorge Oksenberg's lab at UCSF for data analysis. We thank Wenjie Mao in Dr. Lennart Mucke's lab at Gladstone Institute for discussing on behavior tests. We thank Blaise Ndjamen in Gladstone Histology and Light Microscopy Core for helping with confocal imaging and Imaris data analysis. We thank Dr. Wenqing Li in UCSD for comments and editing on this manuscript. The work has also been supported by R56 MH119435 (SJP), NIH/NIMH R01MH122471 (SJP, MRW), UCSF Weill Institute for Neurosciences Innovation Award (SJP, MRW), Marcus Program in Precision Medicine Innovation Transformative Integrated Research Initiative (SJP, MRW), and the Program for Breakthrough Biomedical Research New Frontiers Research Award (SJP, MRW) which is partially funded by the Sandler Foundation. C.M.B is supported by the Hanna H. Gray Fellowship, HHMI and University of California President's Postdoctoral Fellowship Program. A.L.G. was supported by the NMSS Clinician-Scientist Development Award, Kathleen C. Moore Postdoctoral Fellowship. We thank the patient for his participation in research.

## Declaration of interests

The authors declare no competing interests.

## References

Alcami, P., and El Hady, A. (2019). Axonal Computations. Front Cell Neurosci *13*, 413.

Baizabal-Carvallo, J.F., Stocco, A., Muscal, E., and Jankovic, J. (2013). The spectrum of movement disorders in children with anti-NMDA receptor encephalitis. Mov Disord *28*, 543-547.

Bartels, F., Krohn, S., Nikolaus, M., Johannsen, J., Wickstrom, R., Schimmel, M., Hausler, M., Berger, A., Breu, M., Blankenburg, M.*, et al.* (2020). Clinical and Magnetic Resonance Imaging Outcome Predictors in Pediatric Anti-N-Methyl-D-Aspartate Receptor Encephalitis. Ann Neurol *88*, 148-159.

Bird, A.D., and Cuntz, H. (2019). Dissecting Sholl Analysis into Its Functional Components. Cell Rep *27*, 3081-3096 e3085.

Castillo-Gomez, E., Oliveira, B., Tapken, D., Bertrand, S., Klein-Schmidt, C., Pan, H., Zafeiriou, P., Steiner, J., Jurek, B., Trippe, R.*, et al.* (2017). All naturally occurring autoantibodies against the NMDA receptor subunit NR1 have pathogenic potential irrespective of epitope and immunoglobulin class. Mol Psychiatry *22*, 1776-1784.

Dalmau, J. (2016). NMDA receptor encephalitis and other antibody-mediated disorders of the synapse: The 2016 Cotzias Lecture. Neurology *87*, 2471-2482.

Dalmau, J., and Graus, F. (2018). Antibody-Mediated Encephalitis. N Engl J Med *378*, 840-851.

Dalmau, J., Lancaster, E., Martinez-Hernandez, E., Rosenfeld, M.R., and Balice-Gordon, R. (2011). Clinical experience and laboratory investigations in patients with anti-NMDAR encephalitis. Lancet Neurol *10*, 63-74.

Dalmau, J., Tuzun, E., Wu, H.Y., Masjuan, J., Rossi, J.E., Voloschin, A., Baehring, J.M., Shimazaki, H., Koide, R., King, D., *et al.* (2007). Paraneoplastic anti-N-methyl-D-aspartate receptor encephalitis associated with ovarian teratoma. Annals of neurology *61*, 25-36.

Dalva, M.B., Takasu, M.A., Lin, M.Z., Shamah, S.M., Hu, L., Gale, N.W., and Greenberg, M.E. (2000). EphB receptors interact with NMDA receptors and regulate excitatory synapse formation. Cell *103*, 945-956.

Dingledine, R., Borges, K., Bowie, D., and Traynelis, S.F. (1999). The glutamate receptor ion channels. Pharmacological reviews *51*, 7-61.

Du, L., Wang, H., Zhou, H., Chang, H., Wei, Y., Cong, H., Xu, W., Ma, Y., Song, T., Zhang, X., *et al.* (2020). Anti-NMDA receptor encephalitis concomitant with myelin oligodendrocyte glycoprotein antibody diseases: A retrospective observational study. Medicine (Baltimore) *99*, e21238.

Duan, B.C., Weng, W.C., Lin, K.L., Wong, L.C., Li, S.T., Hsu, M.H., Lin, J.J., Fan, P.C., Lin, M.I., Chiu, N.C., *et al.* (2016). Variations of movement disorders in anti-N-methyl-D-aspartate receptor encephalitis: A nationwide study in Taiwan. Medicine (Baltimore) *95*, e4365.

Edwards, T.J., Sherr, E.H., Barkovich, A.J., and Richards, L.J. (2014). Clinical, genetic and imaging findings identify new causes for corpus callosum development syndromes. Brain : a journal of neurology *137*, 1579-1613.

Eggers, E.L., Michel, B.A., Wu, H., Wang, S.-z., Bevan, C.J., Abounasr, A., Pierson, N.S., Bischof, A., Kazer, M., Leitner, E., *et al.* (2017). Clonal relationships of CSF B cells in treatment-naive multiple sclerosis patients. JCI Insight *2*.

Finke, C., Kopp, U.A., Scheel, M., Pech, L.M., Soemmer, C., Schlichting, J., Leypoldt, F., Brandt, A.U., Wuerfel, J., Probst, C., *et al.* (2013). Functional and structural brain changes in anti-N-methyl-D-aspartate receptor encephalitis. Ann Neurol *74*, 284-296.

Florance, N.R., Davis, R.L., Lam, C., Szperka, C., Zhou, L., Ahmad, S., Campen, C.J., Moss, H., Peter, N., Gleichman, A.J., *et al.* (2009). Anti-N-methyl-D-aspartate receptor (NMDAR) encephalitis in children and adolescents. Ann Neurol *66*, 11-18.

Garcia-Serra, A., Radosevic, M., Pupak, A., Brito, V., Rios, J., Aguilar, E., Maudes, E., Arino, H., Spatola, M., Mannara, F., *et al.* (2021). Placental transfer of NMDAR antibodies causes reversible alterations in mice. Neurol Neuroimmunol Neuroinflamm *8*.

Gleichman, A.J., Spruce, L.A., Dalmau, J., Seeholzer, S.H., and Lynch, D.R. (2012). Anti-NMDA receptor encephalitis antibody binding is dependent on amino acid identity of a small region within the GluN1 amino terminal domain. J Neurosci *32*, 11082-11094.

Goldberg, E.M., Titulaer, M., de Blank, P.M., Sievert, A., and Ryan, N. (2014). Anti-N-methyl-D-aspartate receptor-mediated encephalitis in infants and toddlers: case report and review of the literature. Pediatr Neurol *50*, 181-184.

Gordon-Lipkin, E., Yeshokumar, A.K., Saylor, D., Arenivas, A., and Probasco, J.C. (2017). Comparative Outcomes in Children and Adults With Anti- N-Methyl-D-Aspartate (anti-NMDA) Receptor Encephalitis. J Child Neurol *32*, 930-935.

Gresa-Arribas, N., Titulaer, M.J., Torrents, A., Aguilar, E., McCracken, L., Leypoldt, F., Gleichman, A.J., Balice-Gordon, R., Rosenfeld, M.R., Lynch, D., *et al.* (2014). Antibody titres at diagnosis and during follow-up of anti-NMDA receptor encephalitis: a retrospective study. Lancet Neurol *13*, 167-177.

Hacohen, Y., Absoud, M., Hemingway, C., Jacobson, L., Lin, J.P., Pike, M., Pullaperuma, S., Siddiqui, A., Wassmer, E., Waters, P., *et al.* (2014a). NMDA receptor antibodies associated with distinct white matter syndromes. Neurol Neuroimmunol Neuroinflamm *1*, e2.

Hacohen, Y., Dlamini, N., Hedderly, T., Hughes, E., Woods, M., Vincent, A., and Lim, M. (2014b). N-methyl-D-aspartate receptor antibody-associated movement disorder without encephalopathy. Dev Med Child Neurol *56*, 190-193.

Hengst, M., Tucke, J., Zerres, K., Blaum, M., and Hausler, M. (2010). Megalencephaly, mega corpus callosum, and complete lack of motor development: delineation of a rare syndrome. American journal of medical genetics Part A *152A*, 2360-2364.

Hughes, E.G., Peng, X., Gleichman, A.J., Lai, M., Zhou, L., Tsou, R., Parsons, T.D., Lynch, D.R., Dalmau, J., and Balice-Gordon, R.J. (2010). Cellular and synaptic mechanisms of anti-NMDA receptor encephalitis. J Neurosci *30*, 5866-5875.

Iwamura, Y. (2000). Bilateral receptive field neurons and callosal connections in the somatosensory cortex. Philos Trans R Soc Lond B Biol Sci *355*, 267-273.

Iwamura, Y., Taoka, M., and Iriki, A. (2001). Bilateral activity and callosal connections in the somatosensory cortex. Neuroscientist *7*, 419-429.

Jan, S., and Anilkumar, A.C. (2021). Atypical Brain MRI Findings in a Child With Delayed Diagnosis of Anti-N-Methyl-D-Aspartate Receptor Encephalitis. Cureus *13*, e18103.

Jirkof, P. (2014). Burrowing and nest building behavior as indicators of well-being in mice. J Neurosci Methods *234*, 139-146.

Jones, B.E., Tovar, K.R., Goehring, A., Jalali-Yazdi, F., Okada, N.J., Gouaux, E., and Westbrook, G.L. (2019). Autoimmune receptor encephalitis in mice induced by active immunization with conformationally stabilized holoreceptors. Science translational medicine *11*.

Joubert, B., Garcia-Serra, A., Planaguma, J., Martinez-Hernandez, E., Kraft, A., Palm, F., Iizuka, T., Honnorat, J., Leypoldt, F., Graus, F.*, et al.* (2020). Pregnancy outcomes in anti-NMDA receptor encephalitis: Case series. Neurol Neuroimmunol Neuroinflamm *7*.

Jurek, B., Chayka, M., Kreye, J., Lang, K., Kraus, L., Fidzinski, P., Kornau, H.C., Dao, L.M., Wenke, N.K., Long, M.*, et al.* (2019). Human gestational N-methyl-d-aspartate receptor autoantibodies impair neonatal murine brain function. Ann Neurol *86*, 656-670.

Kayser, M.S., and Dalmau, J. (2011). Anti-NMDA Receptor Encephalitis in Psychiatry. Curr Psychiatry Rev *7*, 189-193.

Kreye, J., Wenke, N.K., Chayka, M., Leubner, J., Murugan, R., Maier, N., Jurek, B., Ly, L.T., Brandl, D., Rost, B.R.*, et al.* (2016). Human cerebrospinal fluid monoclonal N-methyl-D-aspartate receptor autoantibodies are sufficient for encephalitis pathogenesis. Brain *139*, 2641-2652.

Lancaster, E. (2016). The Diagnosis and Treatment of Autoimmune Encephalitis. J Clin Neurol *12*, 1-13.

Liu, X.B., Murray, K.D., and Jones, E.G. (2004). Switching of NMDA receptor 2A and 2B subunits at thalamic and cortical synapses during early postnatal development. The Journal of neuroscience : the official journal of the Society for Neuroscience *24*, 8885-8895.

Monyer, H., Burnashev, N., Laurie, D.J., Sakmann, B., and Seeburg, P.H. (1994). Developmental and regional expression in the rat brain and functional properties of four NMDA receptors. Neuron *12*, 529-540.

Moscato, E.H., Peng, X., Jain, A., Parsons, T.D., Dalmau, J., and Balice-Gordon, R.J. (2014). Acute mechanisms underlying antibody effects in anti-N-methyl-D-aspartate receptor encephalitis. Annals of neurology *76*, 108-119.

Nolt, M.J., Lin, Y., Hruska, M., Murphy, J., Sheffler-Colins, S.I., Kayser, M.S., Passer, J., Bennett, M.V., Zukin, R.S., and Dalva, M.B. (2011). EphB controls NMDA receptor function and synaptic targeting in a subunit-specific manner. J Neurosci *31*, 5353-5364.

Paoletti, P., Bellone, C., and Zhou, Q. (2013). NMDA receptor subunit diversity: impact on receptor properties, synaptic plasticity and disease. Nature reviews Neuroscience *14*, 383-400.

Paul, L.K. (2011). Developmental malformation of the corpus callosum: a review of typical callosal development and examples of developmental disorders with callosal involvement. Journal of neurodevelopmental disorders *3*, 3-27.

Peer, M., Pruss, H., Ben-Dayan, I., Paul, F., Arzy, S., and Finke, C. (2017). Functional connectivity of large-scale brain networks in patients with anti-NMDA receptor encephalitis: an observational study. Lancet Psychiatry *4*, 768-774.

Picelli, S., Faridani, O.R., Björklund, Å.K., Winberg, G., Sagasser, S., and Sandberg, R. (2014). Full-length RNA-seq from single cells using Smart-seq2. Nature Protocols *9*, 171.

Planaguma, J., Haselmann, H., Mannara, F., Petit-Pedrol, M., Grunewald, B., Aguilar, E., Ropke, L., Martin-Garcia, E., Titulaer, M.J., Jercog, P.*, et al.* (2016). Ephrin-B2 prevents N-methyl-D-aspartate receptor antibody effects on memory and neuroplasticity. Ann Neurol *80*, 388-400.

Planaguma, J., Leypoldt, F., Mannara, F., Gutierrez-Cuesta, J., Martin-Garcia, E., Aguilar, E., Titulaer, M.J., Petit-Pedrol, M., Jain, A., Balice-Gordon, R.*, et al.* (2015). Human N-methyl D-aspartate receptor antibodies alter memory and behaviour in mice. Brain : a journal of neurology *138*, 94-109.

Ramberger, M., Berretta, A., Tan, J.M.M., Sun, B., Michael, S., Yeo, T., Theorell, J., Bashford-Rogers, R., Paneva, S., O'Dowd, V.*, et al.* (2020). Distinctive binding properties of human monoclonal LGI1 autoantibodies determine pathogenic mechanisms. Brain : a journal of neurology.

Sans, N.A., Montcouquiol, M.E., and Raymond, J. (2000). Postnatal developmental changes in AMPA and NMDA receptors in the rat vestibular nuclei. Brain research Developmental brain research *123*, 41-52.

Semple, B.D., Blomgren, K., Gimlin, K., Ferriero, D.M., and Noble-Haeusslein, L.J. (2013). Brain development in rodents and humans: Identifying benchmarks of maturation and vulnerability to injury across species. Progress in neurobiology *106-107*, 1-16.

Sheng, M., Cummings, J., Roldan, L.A., Jan, Y.N., and Jan, L.Y. (1994). Changing subunit composition of heteromeric NMDA receptors during development of rat cortex. Nature *368*, 144-147.

Tiller, T., Meffre, E., Yurasov, S., Tsuiji, M., Nussenzweig, M.C., and Wardemann, H. (2008a). Efficient generation of monoclonal antibodies from single human B cells by single cell RT-PCR and expression vector cloning. J Immunol Methods *329*, 112-124.

Tiller, T., Meffre, E., Yurasov, S., Tsuiji, M., Nussenzweig, M.C., and Wardemann, H. (2008b). Efficient generation of monoclonal antibodies from single human B cells by single cell RT-PCR and expression vector cloning. Journal of immunological methods *329*, 112-124.

Titulaer, M.J., McCracken, L., Gabilondo, I., Armangue, T., Glaser, C., Iizuka, T., Honig, L.S., Benseler, S.M., Kawachi, I., Martinez-Hernandez, E.*, et al.* (2013). Treatment and prognostic factors for long-term outcome in patients with anti-NMDA receptor encephalitis: an observational cohort study. Lancet Neurol *12*, 157-165.

Varley, J.A., Webb, A.J.S., Balint, B., Fung, V.S.C., Sethi, K.D., Tijssen, M.A.J., Lynch, T., Mohammad, S.S., Britton, F., Evans, M.*, et al.* (2019). The Movement disorder associated with NMDAR antibody-encephalitis is complex and characteristic: an expert video-rating study. J Neurol Neurosurg Psychiatry *90*, 724-726.

Vogt, D., Wu, P.R., Sorrells, S.F., Arnold, C., Alvarez-Buylla, A., and Rubenstein, J.L. (2015). Viral-mediated Labeling and Transplantation of Medial Ganglionic Eminence (MGE) Cells for In Vivo Studies. Journal of visualized experiments : JoVE.

Wang, Y., Miao, A., Shi, Y., Ge, J., Wang, L., Yu, C., Xu, H., Yu, Y., Huang, S., Li, Y.*, et al.* (2020). Influencing electroclinical features and prognostic factors in patients with anti-NMDAR encephalitis: a cohort follow-up study in Chinese patients. Sci Rep *10*, 10753.

Wurdemann, T., Kersten, M., Tokay, T., Guli, X., Kober, M., Rohde, M., Porath, K., Sellmann, T., Bien, C.G., Kohling, R.*, et al.* (2016). Stereotactic injection of cerebrospinal fluid from anti-NMDA receptor encephalitis into rat dentate gyrus impairs NMDA receptor function. Brain research *1633*, 10-18.

Yeh, E.A. (2014). White matter changes in childhood NMDA receptor encephalitis: Bringing new light to an old phenotype. Neurol Neuroimmunol Neuroinflamm *1*, e3.

Yeshokumar, A., Gordon-Lipkin, E., Arenivas, A., Rosenfeld, M., Patterson, K., Blum, R., Banwell, B., Venkatesan, A., Lancaster, E., Panzer, J.*, et al.* (2022). Younger Age at Onset Is Associated With Worse

Long-term Behavioral Outcomes in Anti-NMDA Receptor Encephalitis. Neurol Neuroimmunol Neuroinflamm *9*.

Zhou, J., Lin, Y., Huynh, T., Noguchi, H., Bush, J.O., and Pleasure, S.J. (2021). NMDA receptors control development of somatosensory callosal axonal projections. Elife *10*.

Zhou, J., Wen, Y., She, L., Sui, Y.N., Liu, L., Richards, L.J., and Poo, M.M. (2013). Axon position within the corpus callosum determines contralateral cortical projection. Proc Natl Acad Sci U S A *110*, E2714-2723.

## Figures and Figure legends

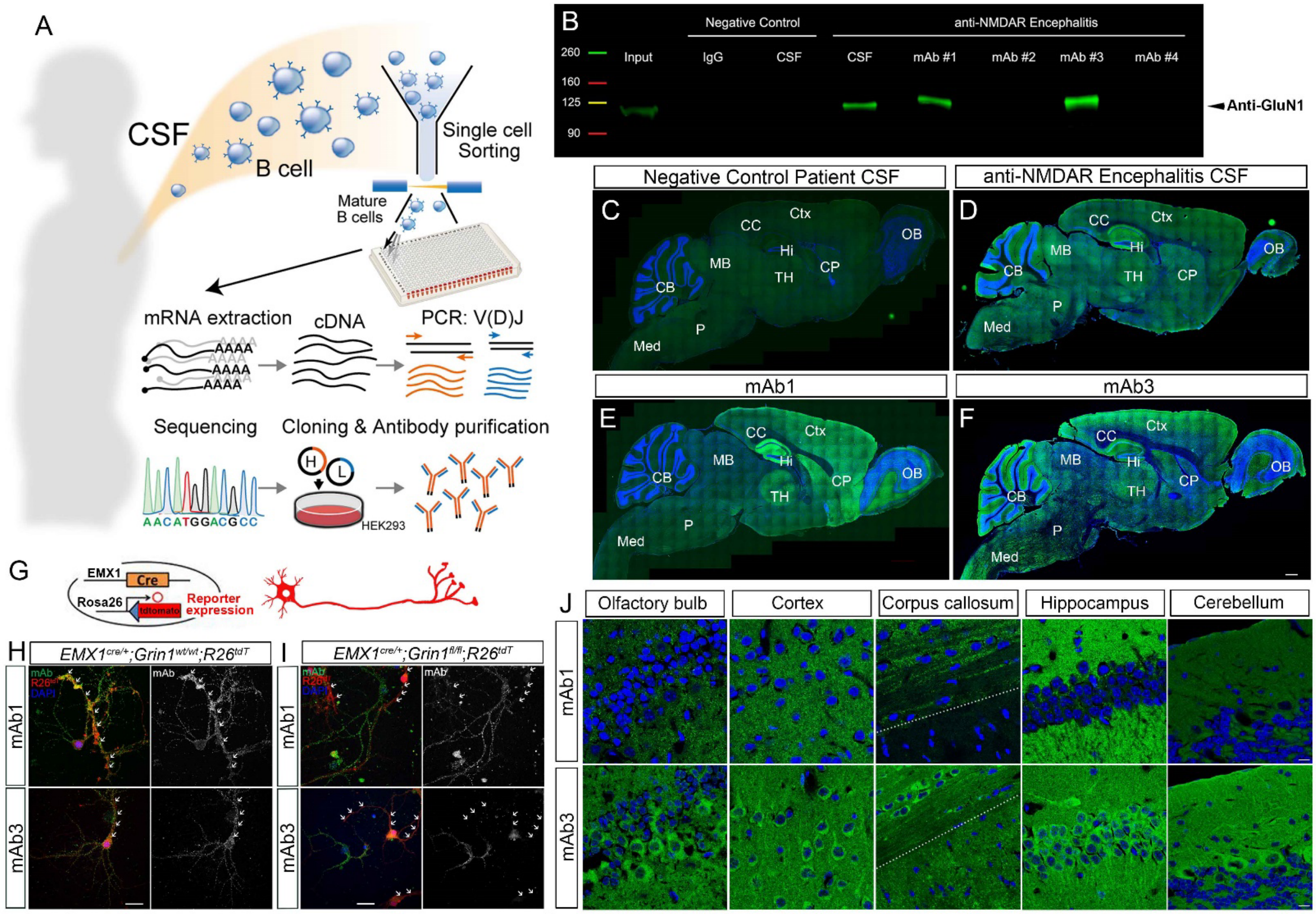
A
CSF
B cell
Single cell Sorting
Mature B cells
mRNA extraction
cDNA
PCR: V(D)J
AAAA
Sequencing
Cloning & Antibody purification
AACATGGACGCC
H
L
HEK293
B
Negative Control
anti-NMDAR Encephalitis
Input
IgG
CSF
CSF
mAb #1
mAb #2
mAb #3
mAb #4
260
160
125
90
Anti-GluN1
Negative Control Patient CSF
anti-NMDAR Encephalitis CSF
C
D
mAb1
mAb3
E
F
CC
Ctx
Hi
TH
CP
OB
MB
CB
P
Med
G
EMX1
Cre
Rosa26
tdtomato
Reporter expression
H
EMX1cre/+;Grin1wt/wt;R26tdT
I
EMX1cre/+;Grin1fl/fl;R26tdT
mAb
R26tdT
DAPI
mAb1
mAb3
J
Olfactory bulb
Cortex
Corpus callosum
Hippocampus
Cerebellum
mAb1
mAb3

**Figure 1**: **Generation of patient-derived monoclonal anti-NMDAR antibodies.** (A) Diagram of generation of patient-derived monoclonal anti-NMDAR antibodies. (B) Immunoprecipitation of GluN1 from postnatal day 40 (P40) mouse brain homogenates by using anti-NMDAR encephalitis patient's CSF, mAb1, mAb2, mAb3 and mAb4. Immunoprecipitation with human IgG, nonanti-NMDAR encephalitis patient's CSF served as negative controls. (C-F) Immunostaining with CSF of negative control patient (C), CSF of anti-NMDAR encephalitis patient (D), mAb1 (E) and mAb3 (F) on sagittal sections of P40 mouse brains. The staining of control patient CSF served as negative control. (G-I) mAb1 and mAb3 recognized extracellular epitopes of NMDAR. (G) We crossed *Emx1*$^{cre/+}$; *Grin1*$^{fl/fl}$ mice with Cre-reporter *Rosa26*$^{fs\text{-}tdTomato}$ mice to produce GluN1 knockout cells labled with red fluorescence. Hippocampal neurons were cultured from *Emx1*$^{cre/+}$; *Grin1*$^{fl/fl}$; *Rosa26*$^{fs\text{-}tdTomato}$ mice. Hippocampal cultures of *Emx1*$^{cre/+}$; *Grin1*$^{wt/wt}$; *Rosa26*$^{fs\text{-}tdTomato}$ mice served as controls. (H, I) mAb1 and mAb3 showed punctate membrane staining in live staining of cultured hippocampal neuron. The staining was gone in red cells of *Emx1*$^{cre/+}$; *Grin1*$^{fl/fl}$; *Rosa26*$^{fs\text{-}tdTomato}$ cultures (I) but not red cells of *Emx1*$^{cre/+}$; *Grin1*$^{wt/wt}$; *Rosa26*$^{fs\text{-}}$

*tdTomato* cultures (H). (J) Immunostaining pattern of mAb1 and mAb3 in different brain regions. Dash line is the border line between cortex and corpus callosum. Scale bar: 500µm for images C-F; 50µm for images in H and I; 10µm for images in J. *R26*$^{tdT}$: *Rosa26*$^{fs\text{-}tdTomato}$. OB: olfactory bulb. Ctx: cortex. Hi: hippocampus. CP: Caudoputamen. TH: thalamus. MB: midbrain. CB: cerebellum. P: pons. Med: medulla.

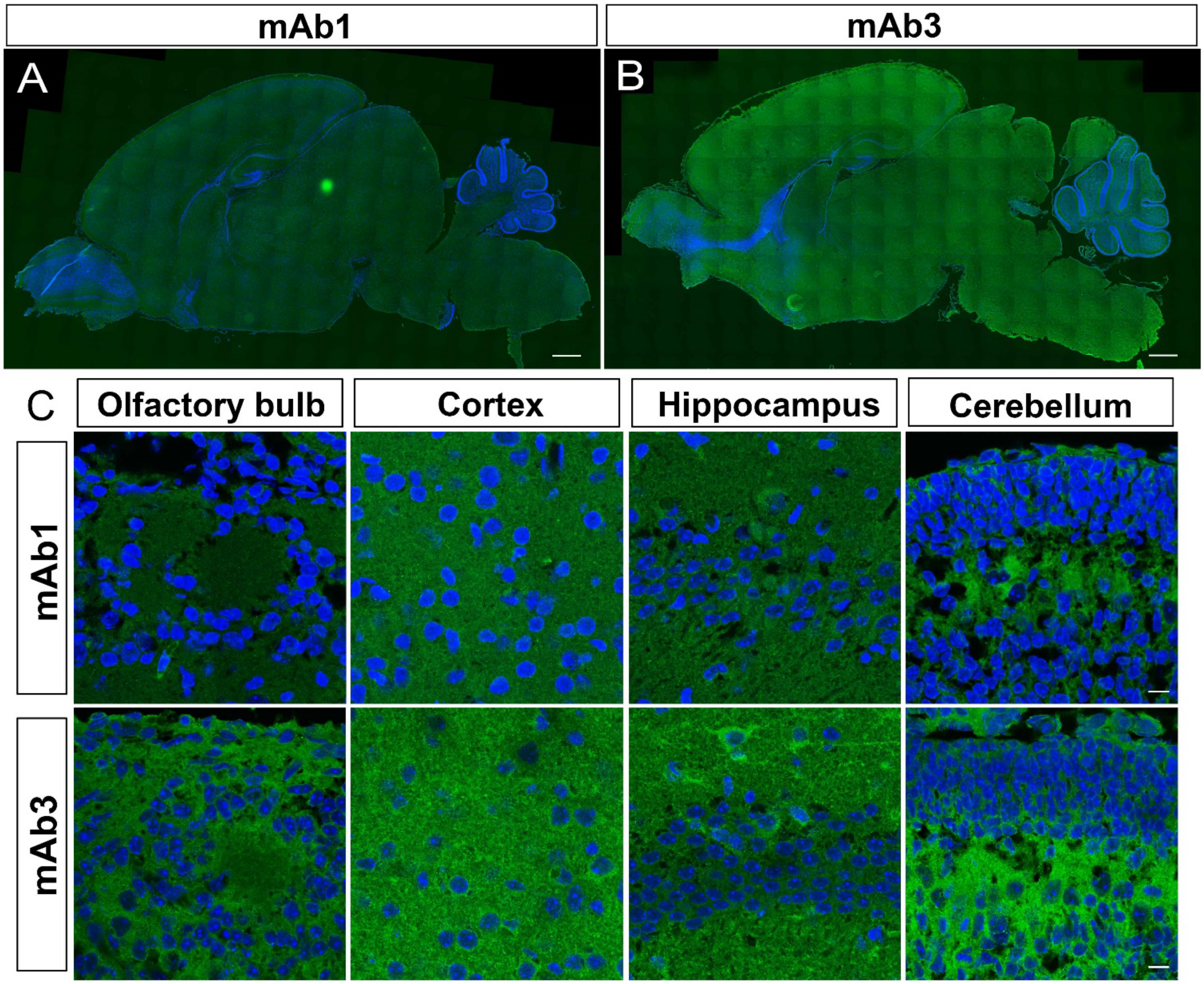

**Figure 1-figure supplementary 1: Immunostaining pattern of mAb1 and mAb3 at early developmental stage**. The immunostaining pattern mAb1 (A) and mAb3 (B) on sagittal sections of P8 mouse brains. (C) Immunostaining pattern of mAb1 and mAb3 in different brain regions. Scale bar: 500µm for images A, and B; 10µm for images in C.

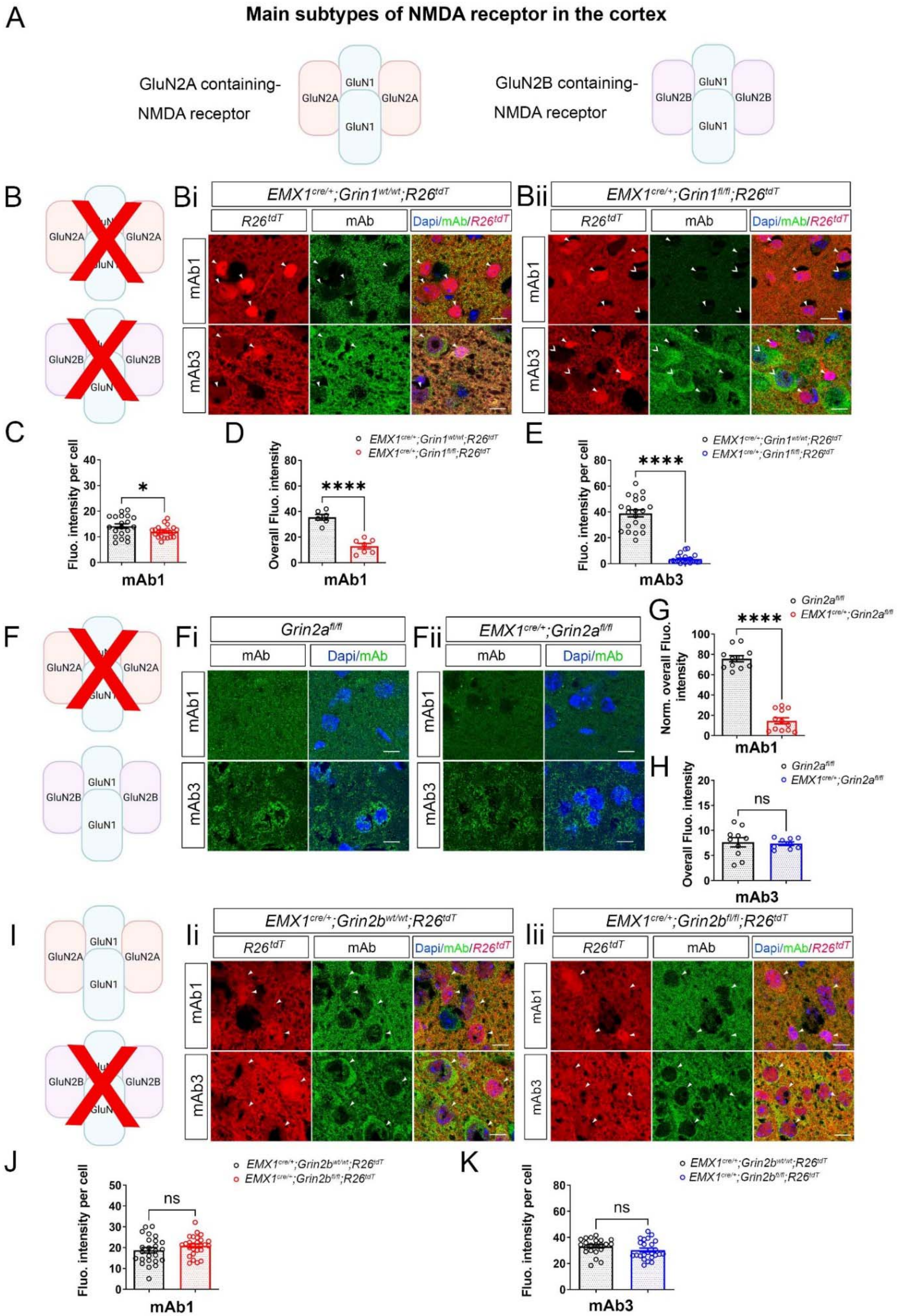
A
Main subtypes of NMDA receptor in the cortex
GluN2A containing-NMDA receptor
GluN1
GluN2A
GluN2B containing-NMDA receptor
GluN2B
B
Bi
EMX1cre/+;Grin1wt/wt;R26tdT
Bii
EMX1cre/+;Grin1fl/fl;R26tdT
R26tdT
mAb
Dapi/mAb/R26tdT
mAb1
mAb3
C
Fluo. intensity per cell
*
D
Overall Fluo. intensity
****
E
F
Fi
Grin2afl/fl
Fii
EMX1cre/+;Grin2afl/fl
Dapi/mAb
G
Norm. overall Fluo. intensity
H
ns
I
Ii
EMX1cre/+;Grin2bwt/wt;R26tdT
Iii
EMX1cre/+;Grin2bfl/fl;R26tdT
J
K

**Figure 2**: **mAb3 binds the GluN1 subunit, while mAb1 binds the GluN2A subunit**. (A) Diagram of GluN2A-containing NMDAR and GluN2B-containing NMDAR. (B-E) We generated *Emx1*$^{cre/+}$; *Grin1*$^{fl/fl}$; *Rosa26*$^{fs\text{-}tdTomato}$ mice to produce NMDAR knockout cells labled with red fluorescence. *Emx1*$^{cre/+}$; *Grin1*$^{wt/wt}$; *Rosa26*$^{fs\text{-}tdTomato}$ mice of the same litter served as control. Immunostaining of mAb1 and mAb3 were done in these brain sections (Bi, Bii). Triangle arrowheads pointed cells with Cre recombination. V shaped arrowheads pointed cells without Cre recombination. The punctate cell membrane and fiber staining of mAb1 were seen in *Emx1*$^{cre/+}$; *Grin1*$^{wt/wt}$; *Rosa26*$^{fs\text{-}tdTomato}$ mice (Bi), but dramatically reduced in *Emx1*$^{cre/+}$; *Grin1*$^{fl/fl}$; *Rosa26*$^{fs\text{-}tdTomato}$ mice (Bii). mAb3 signals were only detected on non-Cre recombination cells but absent on Cre recombination cells with deletion of NMDAR (Bii). (C, D) Quantification of fluorescence intensity of mAb1 immunostaining in single cells (C, P=0.03, n = 20 to 22 per group) and overall image (D, P<0.0001, n = 6 to 7 per group). (E) Quantification of fluorescence intensity of mAb3 immunostaining in single cells (P<0.0001, n = 20 to 21 per group). (F-H) We generated *Emx1*$^{cre/+}$; *Grin2a*$^{fl/fl}$ mice to conditional knock out GluN2A-containing NMDAR in excitatory neurons in cortex. The same littermates *Grin2a*$^{fl/fl}$ mice served as controls. The punctate staining of mAb1 seen in *Grin2a*$^{fl/fl}$ mice were dramatically reduced in *Emx1*$^{cre/+}$; *Grin2a*$^{fl/fl}$ mice (Fii, G (P<0.0001, n = 11 to 12 per group)). However, there were no difference between the signals of mAb3 in *Grin2a*$^{fl/fl}$ mice (F) and *Emx1*$^{cre/+}$; *Grin2a*$^{fl/fl}$ mice (Fii, H (P=0.79, n = 9 to 10 per group)). (I-K) We generated *Emx1*$^{cre/+}$; *Grin2b*$^{fl/fl}$; *Rosa26*$^{fs\text{-}tdTomato}$ mice to produce GluN2B-containing NMDARs knockout cells labled with red fluorescence. The littermates *Emx1*$^{cre/+}$; *Grin2b*$^{wt/wt}$; *Rosa26*$^{fs\text{-}tdTomato}$ mice served as controls. There were no difference between the singals of mAb1 (J, P=0.18, n = 25 to 26 per group) and mAb3 (K, P=0.16, n = 22 to 24 per group) in *Emx1*$^{cre/+}$; *Grin2b*$^{wt/wt}$; *Rosa26*$^{fs\text{-}tdTomato}$ mice (Ii) and *Emx1*$^{cre/+}$; *Grin2b*$^{fl/fl}$; *Rosa26*$^{fs\text{-}tdTomato}$ mice (Iii). Scale bar: 10μm for all images. Above statistics were based on student T test.

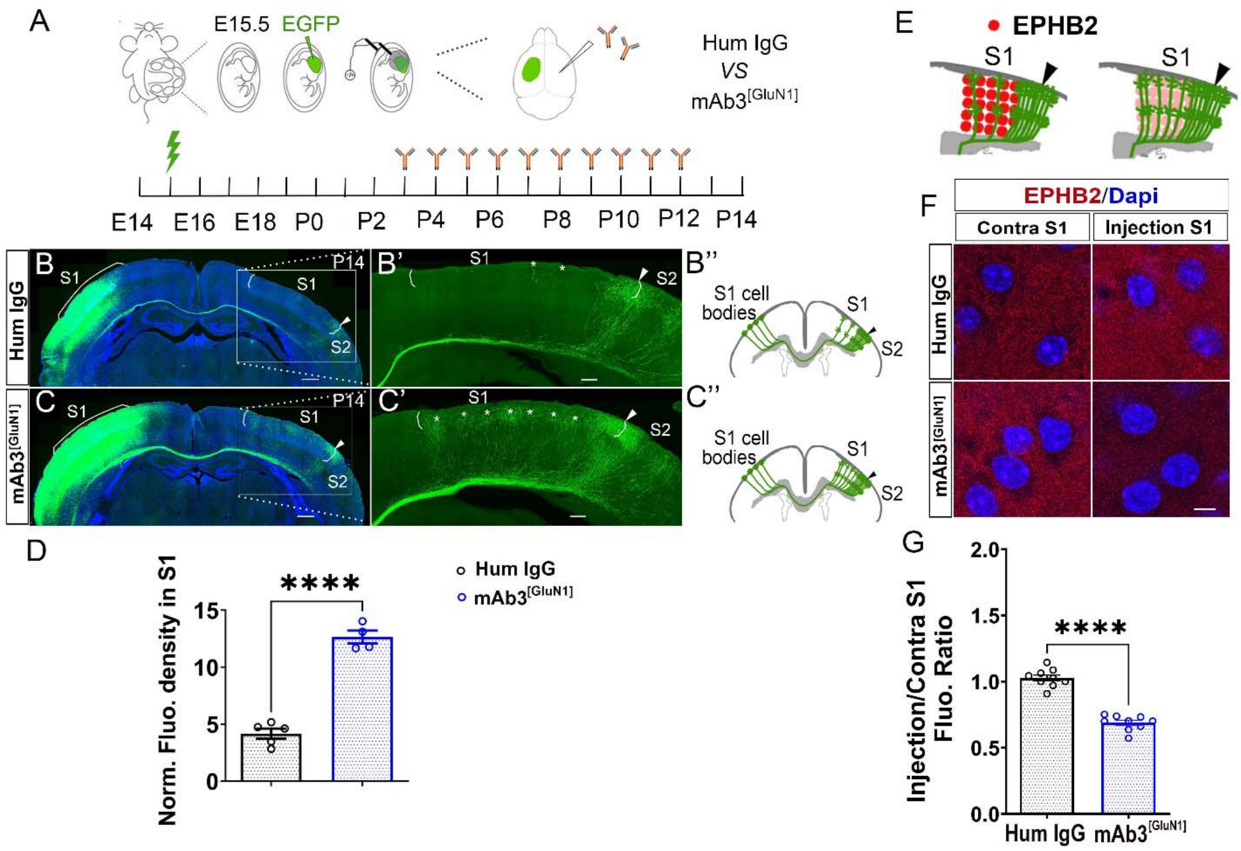
A
E15.5 EGFP
Hum IgG
VS
mAb3[GluN1]
E14 E16 E18 P0 P2 P4 P6 P8 P10 P12 P14
B S1 P14 S1 S2
B' S1 S2
B''
S1 cell bodies
S1
S2
C S1 P14 S1 S2
C' S1 S2
C''
S1 cell bodies
S1
S2
Hum IgG
mAb3[GluN1]
D
Norm. Fluo. density in S1
0
5
10
15
****
○ Hum IgG
○ mAb3[GluN1]
E
● EPHB2
S1
S1
F
EPHB2/Dapi
Contra S1
Injection S1
Hum IgG
mAb3[GluN1]
G
Injection/Contra S1 Fluo. Ratio
0.0
0.5
1.0
1.5
2.0
****
Hum IgG
mAb3[GluN1]

**Figure 3**: **Disrupted callosal projections in primary somatosensory cortex (S1) after intraventricular injection of mAb3$^{[GluN1]}$ from P3 to P12.** (A) Diagram of experimental procedure. EGFP plasmid injected into lateral ventricle of embryo at embryonic day15.5 (E15.5) and electrical pulse given to enable the plasmid to enter cortical progenitor cells of layer II/III in the ventricular zone. mAb3$^{[GluN1]}$ was injected into the lateral ventricle from P3 to P12 in contralateral cortex. Human IgG served as control. Compared with control (B), mAb3$^{[GluN1]}$ injection mice showed dramatically increased callosal projections (C) in S1 at P14. "*" pointed the callosal axons in S1. (D) Quantification of fluorescence density. Human IgG *VS* mAb3$^{[GluN1]}$: $P < 0.0001$. $n = 4$ to 5 per group. (E) Diagram of EPHB2 expression in S1. (F) Expression of EPHB2 in S1 of injecting side and contralateral noninjecting side for the three different treatments. (G) Quantification of fluorescence intensity ratio of injecting side to contralateral noninjecting side. Human IgG *VS* mAb3$^{[GluN1]}$: $P < 0.0001$. $n = 9$ for each group. Scale bar: 500µm for B, B', C, C'; 5µm for F. Above statistics were based on Mann-Whitney test.

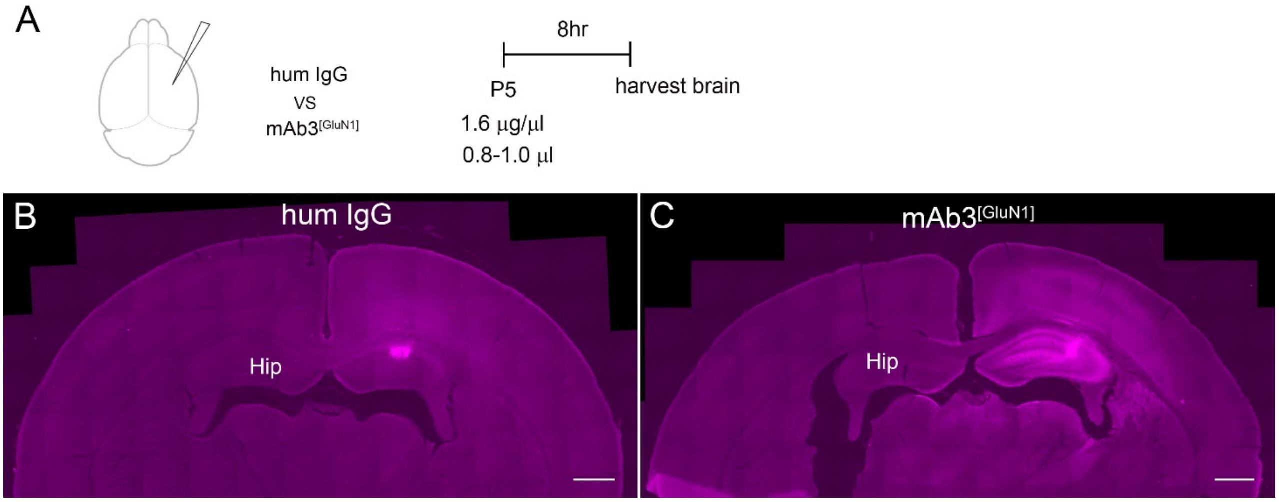
A
hum IgG
vs
mAb3[GluN1]
8hr
P5
harvest brain
1.6 µg/µl
0.8-1.0 µl
B
hum IgG
Hip
C
mAb3[GluN1]
Hip

**Figure 3-figure supplementary 1: The diffusion territory of mAb3$^{[\text{GluN1}]}$ in mouse cortex after 8 hours of intraventricular injection.** (A) We injected mAb3$^{[\text{GluN1}]}$ into the lateral ventricle at P5 and perfused the mouse 8 hours later. The Human IgG were injected into the same littermates as controls. We stained mouse brain with anti-Human secondary antibody coupled to Cy5, which thus indicated where the antibodies had diffused in the mouse brain. (B) In control mice, the Human IgG had diffused to motor and sensory cortexes, but the signal was getting weaker. (C) However, mAb3$^{[\text{GluN1}]}$ injection brain still had strong signals in cortex and hippocampus on the injection side. Scale bar: 500µm for all images. Hip: hippocampus.

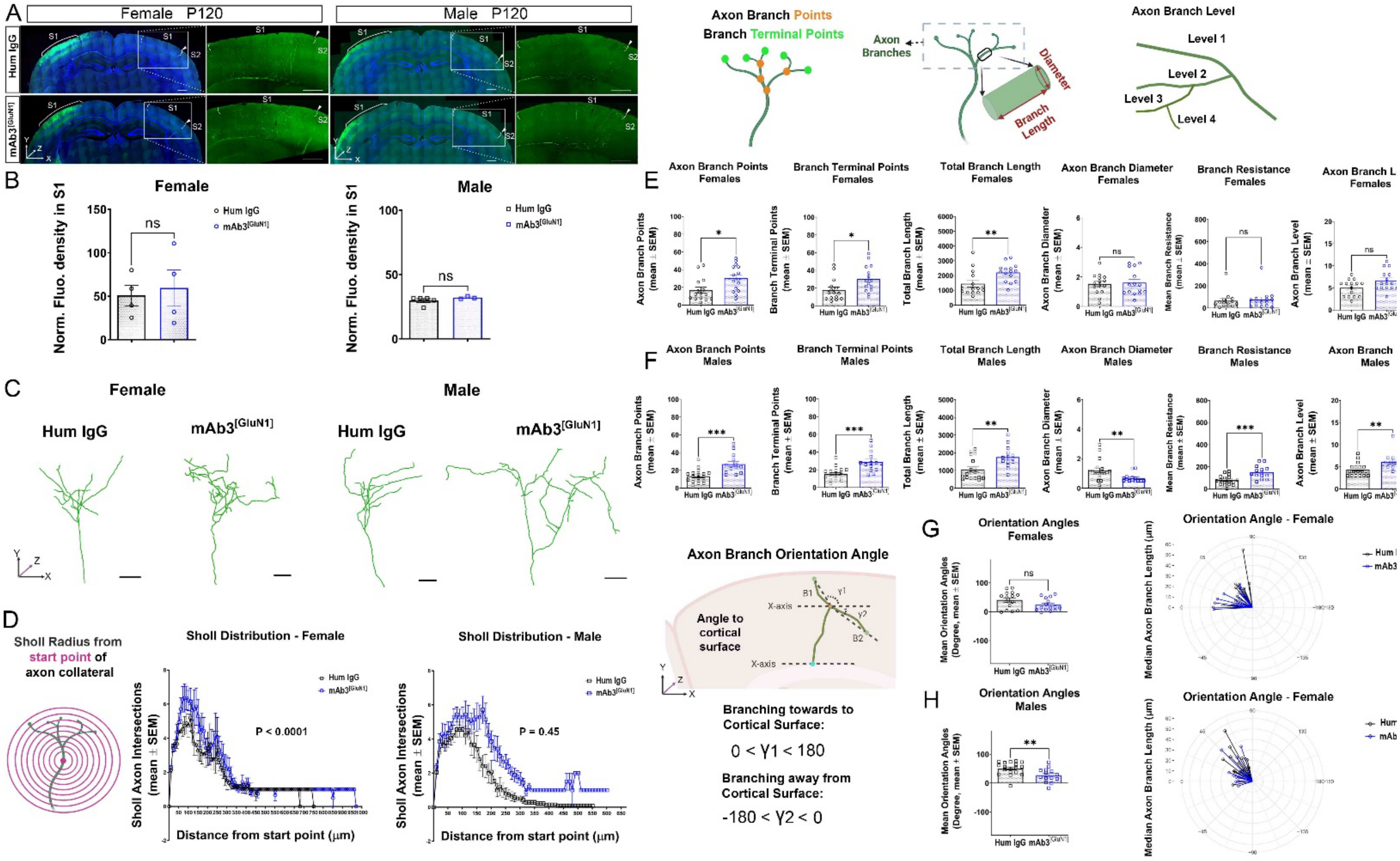

**Figure 4**: **Permanent morphological alterations of S1 callosal axons in mAb3$^{[GluN1]}$-treated mice.** (A) Disrupted callosal projection pattern in S1 caused by mAb3$^{[GluN1]}$ from P3 to P12 during development was recovered when mice were at P120. (B) Quantification of fluorescence density. Human IgG *VS* mAb3$^{[GluN1]}$: P > 0.999 (female); P = 0.87 (male). (C) Represented morphology of individual callosal axon terminals in S1 at P120. (D) Sholl analysis of callosal axon branches in female and male mice. Concentric circles from start point are used to count the numbers of axon intersections. Start point was defined at 10μm before the first branch intersection along the main axon trunk (magenta point in the diagram). (E, F) Morphological features of axon branch terminals in mAb3$^{[GluN1]}$-treated female (E) and male (F) mice. Axon branch orientation angle in female (G) and male (H) mice. The angle forms between extending line connecting distal axon branch segment to x-axis of image within the XY plane. X-axis is parallel to the cortical surface. Angle is from -180 to 180 degree and is used to quantify the extending direction of axon branch to cortical surface. Positive angle (0 - 180) means axon branch is extending towards to cortical surface, while negative angle (-180 - 0) means axon branch is extending away from cortical surface. *$P < 0.05$; **$P < 0.05$; ***$P < 0.01$. n = 3 to 5 per group (B). n = 14 to 18 per group (D-H). Above statistics were based on Mann-Whitney test. The plots in G and H were made in R using ggplot2 package.

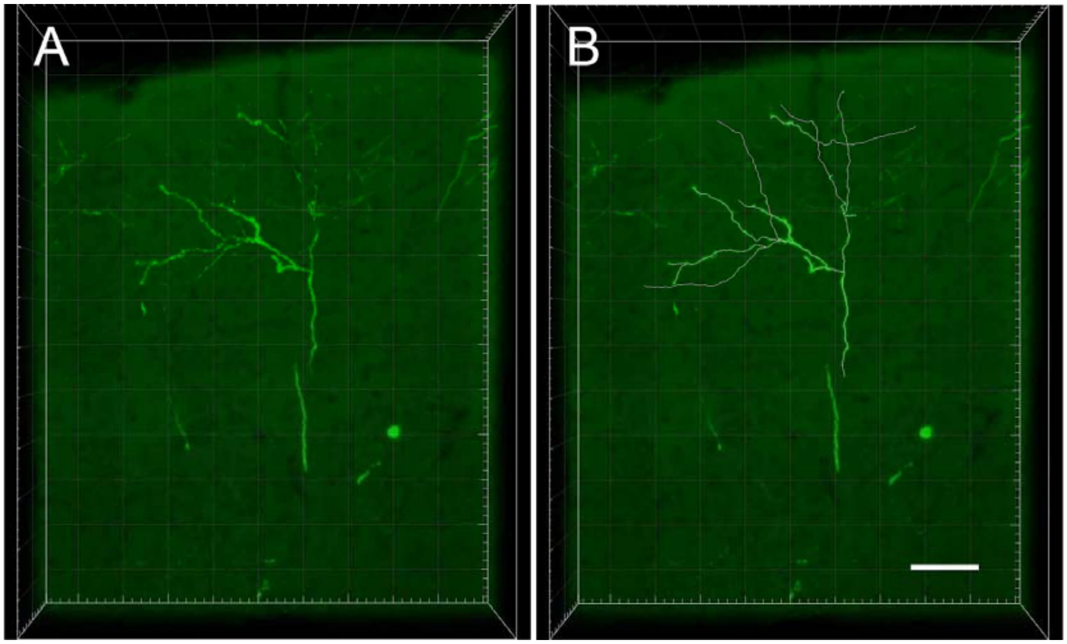

**Figure 4-figure supplementary 1: Axon branches were traced semi-automatically using Imaris software.** (A) 3D confocal image of S1 callosal axon terminals loaded in Imaris. Image was taken from a 200-µm coronal section of P120 mouse brain. (B) The morphology of individual callosal axon terminals was tracked across 3D in Imaris. Traced axon branches in Imaris. The morphology was tracked manually with combining Autopath function in Imaris. Scale bar: 70µm.

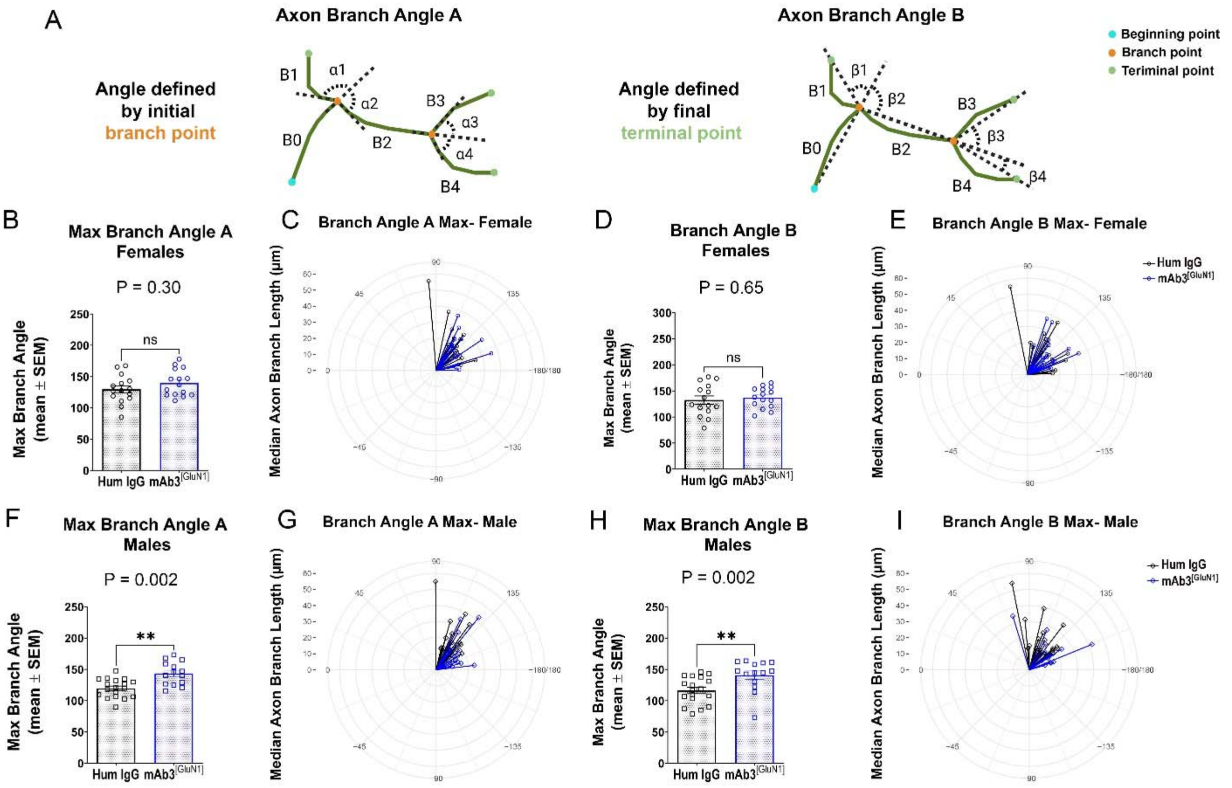

**Figure 4-figure supplementary 2: Significantly increased branch angles in mAb3$^{[GluN1]}$-treated male mice.** (A) Diagram of two ways to measure axon branch angles. Axon branch angle A: defined as the angle between the extending lines from the branch point and its peripheral neighbor vertex. Axon branch angle B: defined as the angle between the extending lines connecting the branch point with the neighboring branch points and the terminal points, respectively. Max branch angle A in female (B, C) and male (F, G) mice. Max branch angle B in female (D, E) and male (H, I) mice. There were significantly increased branch angles in mAb3$^{[GluN1]}$ male mice (F, H) in the two different axon branch angle measurements. n = 14 to 18 per group. The plots in C, E, G, and I were made in R using ggplot2 package. P value on the graph represents the statistically difference between two groups by using Mann-Whitney test.

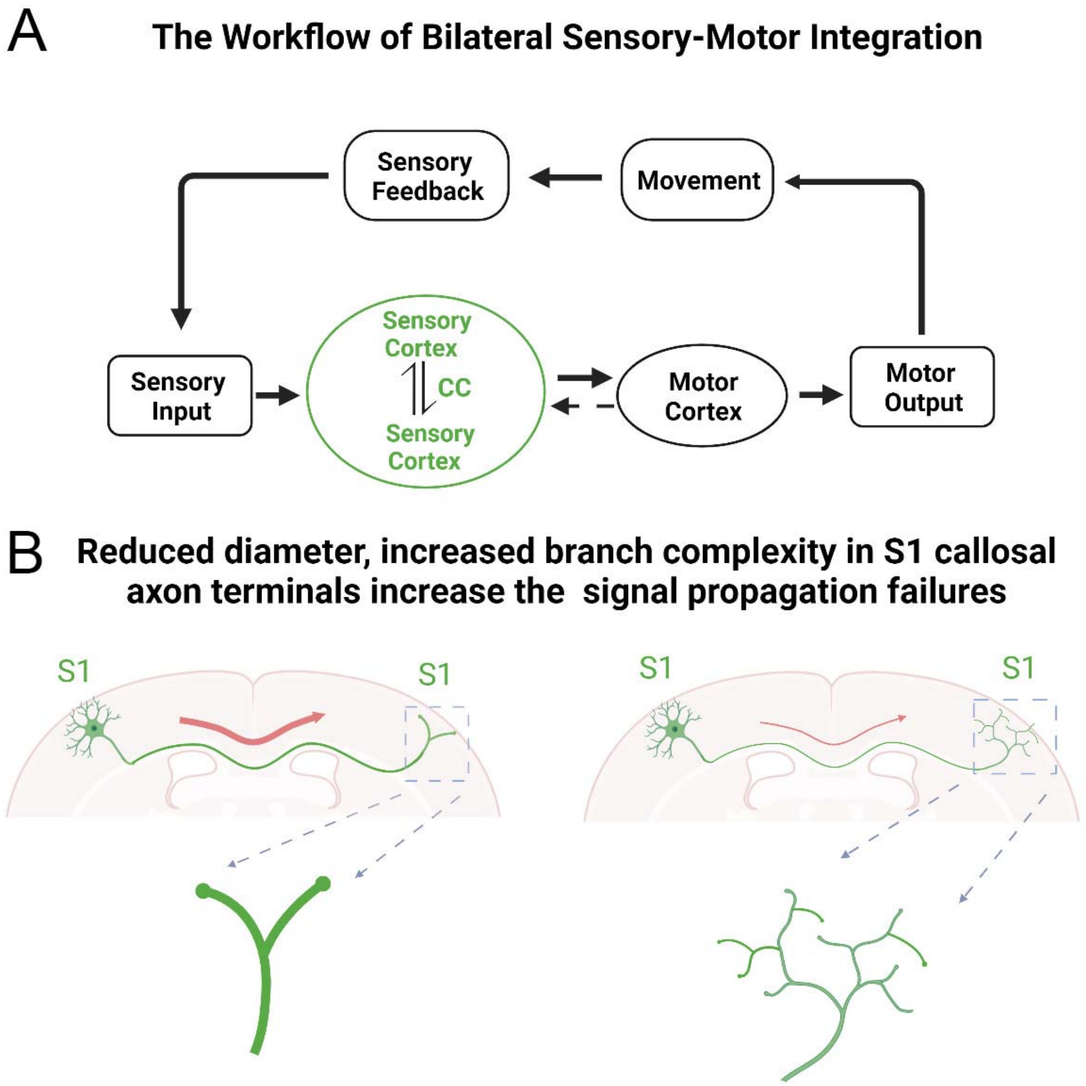
A
The Workflow of Bilateral Sensory-Motor Integration
Sensory Feedback
Movement
Sensory Input
Sensory Cortex
CC
Sensory Cortex
Motor Cortex
Motor Output
B
Reduced diameter, increased branch complexity in S1 callosal axon terminals increase the signal propagation failures
S1
S1
S1
S1

**Figure 4-figure supplementary 3: Model of sensory-motor integration in somatosensory cortex**. (A) Workflow of bilateral sensory-motor integration. (B) Model of morphometric features of callosal axons on sensory signal propagation in somatosensory cortex.

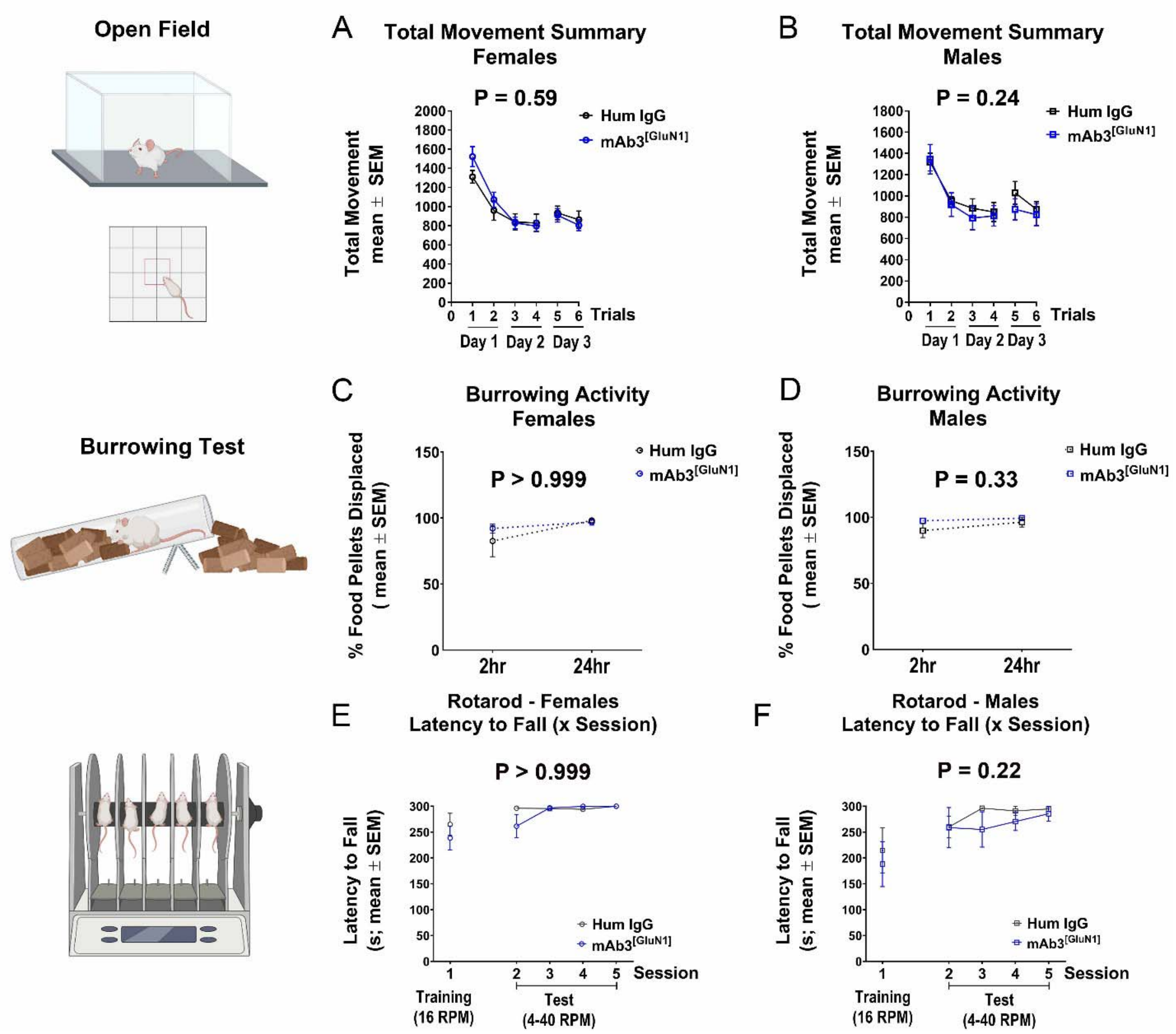

**Figure 5**: **Unaffected coarse movements in mAb3$^{[GluN1]}$-treated mice.** (A, B) Locomotor activity in Open Field Test (OFT). There was no difference of total movements between Human IgG and mAb3$^{[GluN1]}$-treated female (A) and male (B) mice. (C, D) Digging and kicking activity in burrowing test. There was no difference of burrowing performance between two groups in females (C) and males (D) mice. (E, F) Motor coordination in rotarod. There was no difference of rotarod performance between two groups in females (E) and males (F) mice. n = 6 to 8 per group. P value on each figure graph represents the statistically difference between the two groups over Trails by using Two-way Analysis of Variance (ANOVA) and Geisser-GreenHouse correction.

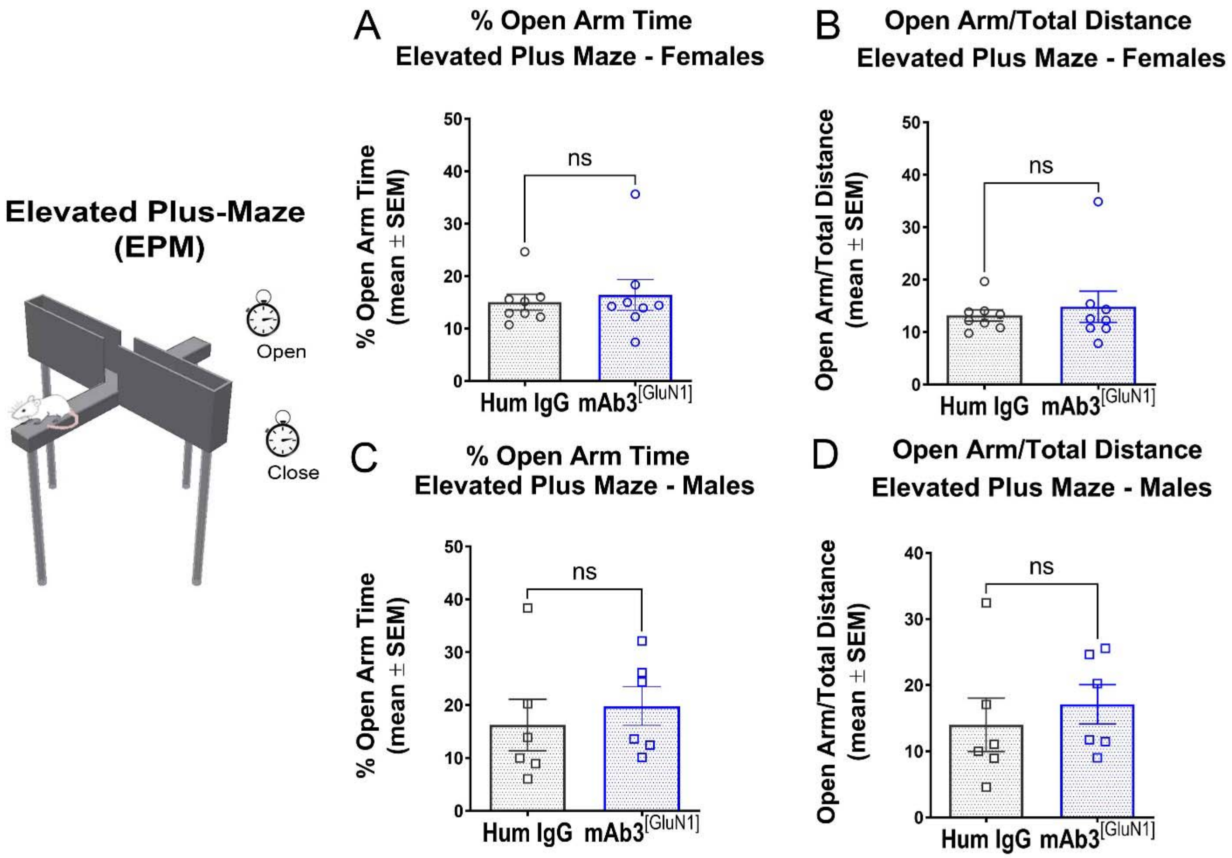

**Figure 5-figure supplementary 1: No increased anxiety in mAb3$^{[GluN1]}$-treated mice.** (A, B) Time traveled in the open arm of Elevated Plus-Maze (EPM). There was no difference of time spending on the open arms between Human IgG and mAb3$^{[GluN1]}$ treated female (A, P = 0.96) and male (B, P > 0.999) mice. (C, D) Distance traveled in the open arm of EPM. There was no difference of distance traveled on the open arms between Human IgG and mAb3$^{[GluN1]}$ treated female (C, P = 0.39) and male (D, P = 0.31) mice. n = 6 to 8 per group. P value represents the statistically difference between two groups by using Mann-Whitney test.

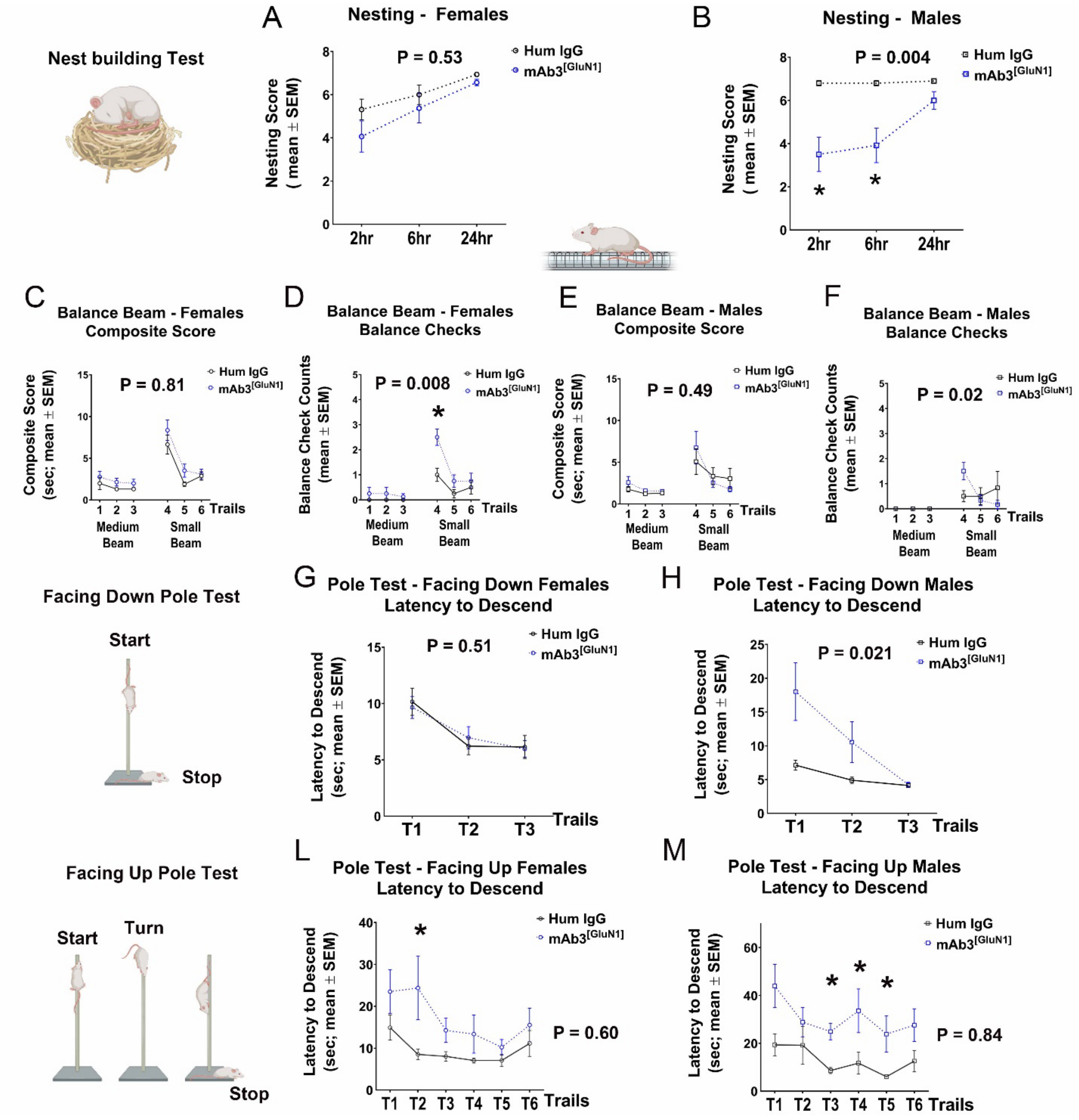

**Figure 6: Persistent impaired fine movements in mAb3$^{[GluN1]}$-treated mice.** (A, B) Nest building. There was significantly impaired nest building in mAb3$^{[GluN1]}$-treated male mice at 2hr (Human IgG *VS* mAb3$^{[GluN1]}$: P = 0.02) and 6hr (Human IgG *VS* mAb3$^{[GluN1]}$: P = 0.03) (B). (C-F) Balance beam. There was no difference in latency of beam crossing for female (C) and male (E) mice. However, there was significantly increased balance check in mAb3$^{[GluN1]}$-treated female mice (D) at Trail 4 (Human IgG *VS* mAb3$^{[GluN1]}$: P = 0.009). (G, H) Facing down pole test. Significantly increased descent latency was observed in mAb3$^{[GluN1]}$-treated male mice over all three trials (H). However, there was no difference in descent latency in each trail for female (G) and male (H) mice. (L, M) Facing up pole test. There was significantly increased descent latency in mAb3$^{[GluN1]}$-treated

female mice (L) at Trail 2 (Human IgG *VS* mAb3$^{[GluN1]}$: P = 0.01), and mAb3$^{[GluN1]}$-treated male (M) at Trail 3 (Human IgG *VS* mAb3$^{[GluN1]}$: P = 0.04), Trail 4 (Human IgG *VS* mAb3$^{[GluN1]}$: P = 0.04), and Trail 5 (Human IgG *VS* mAb3$^{[GluN1]}$: P = 0.03). n = 6 to 8 per group. P value on each figure graph represents the statistically difference between two groups over all Trails by using Two-way ANOVA and Geisser-GreenHouse correction. P value in figure legends represents the statistically difference between two treatments for one Trail by using Dunn's multiple comparisons test.

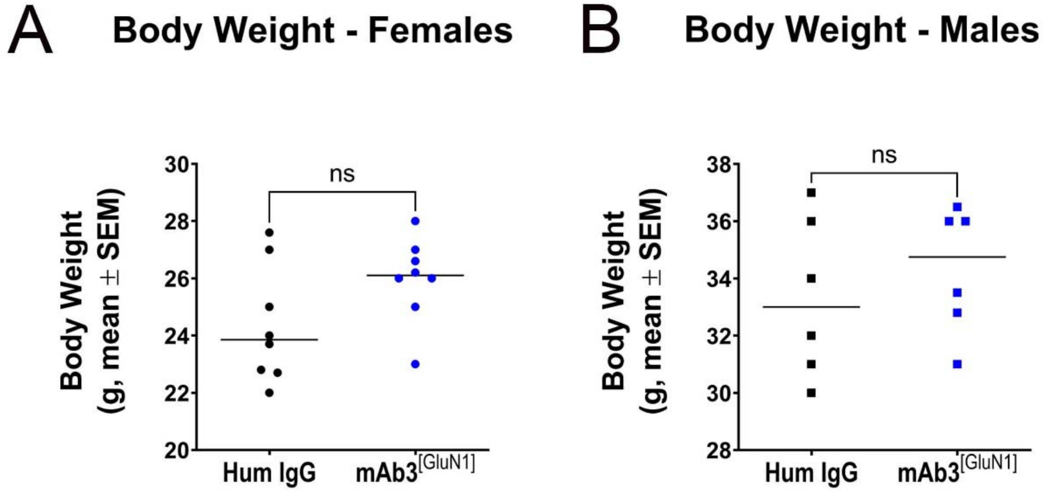

**Figure 6-figure supplementary 1: No body weight difference between groups**. Comparison of body weight in female (A, P = 0.12) and male mice (B, P = 0.62). Above statistics were based on Mann-Whitney test.

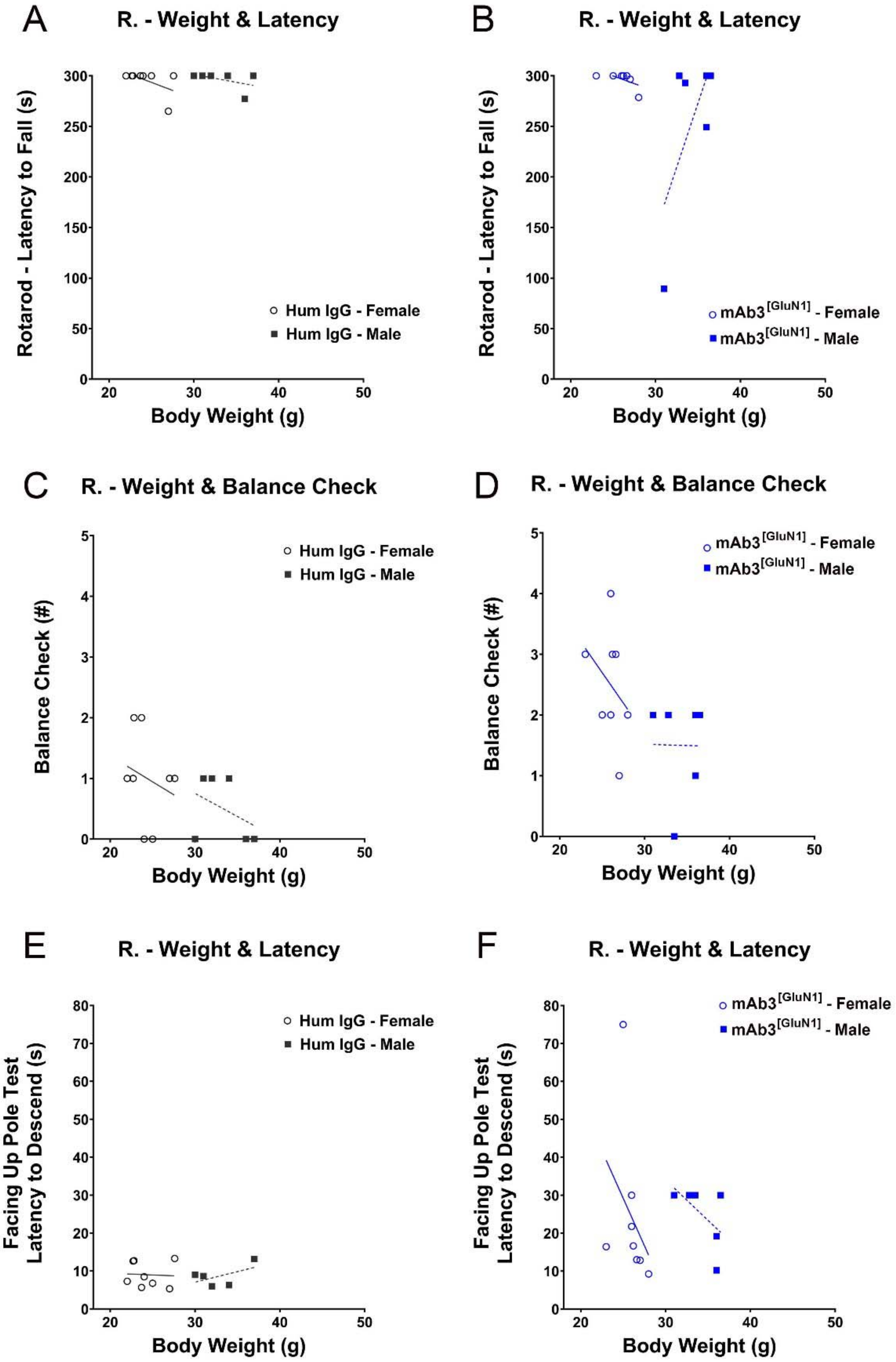

**Figure 6-figure supplementary 2: No correlation between body weight and motor performance.** (A, B) Correlation between weight and Latency to fall (session 2 of rotarod). (A) Human IgG (Female: $R^2 = 0.27$, $P = 0.18$ by linear regression; Male: $R^2 = 0.22$, $P = 0.35$). (B) mAb3$^{[GluN1]}$ (Female: $R^2 = 0.36$, $P = 0.11$; Male: $R^2 =$

0.44, P = 0.15). (C, D) Correlation between weight and balance check (Trail 4 of balance beam). (C) Human IgG (Female: $R^2$ = 0.05, P = 0.58; Male: $R^2$ = 0.15, P = 0.44). (D) mAb3$^{[GluN1]}$ (Female: $R^2$ = 0.10, P = 0.44; Male: $R^2$ = 0.0001, P = 0.98). (E, F) Correlation between weight and Latency to descend (Trail 2 of facing up pole). (E) Human IgG (Female: $R^2$ = 0.003, P = 0.90; Male: $R^2$ = 0.29, P = 0.35). (F) mAb3$^{[GluN1]}$ (Female: $R^2$ = 0.12, P = 0.40; Male: $R^2$ = 0.31, P = 0.25).

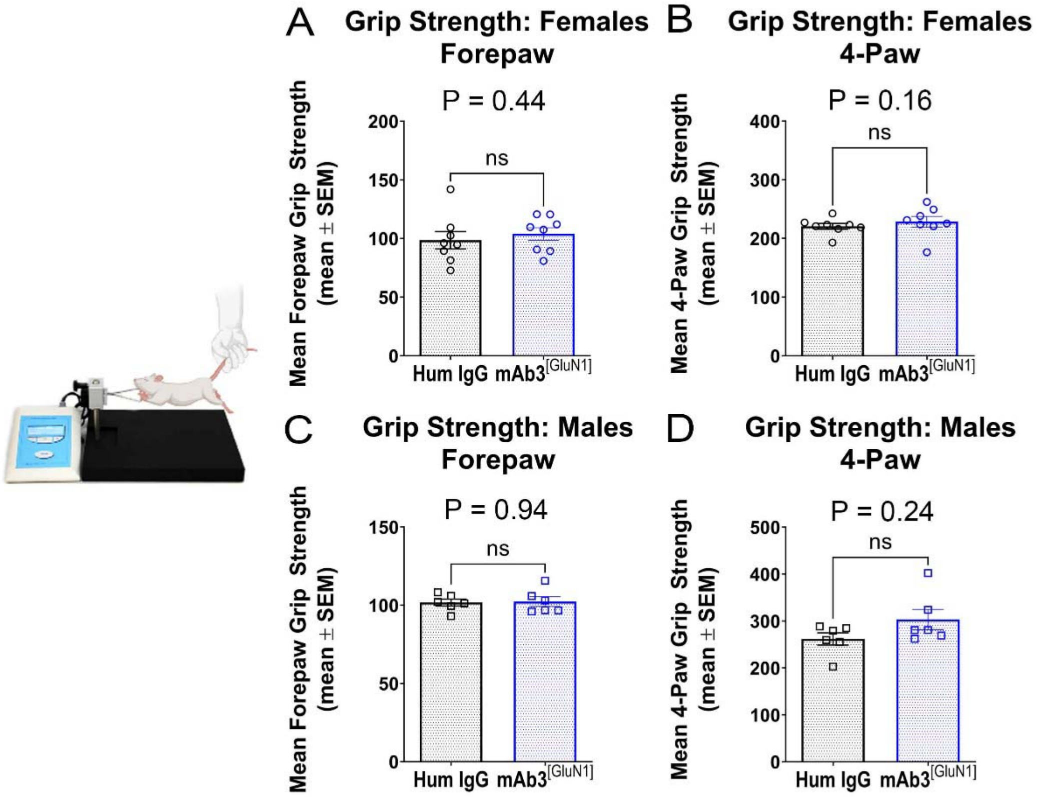

**Figure 6-figure supplementary 3: No impaired muscle strength in mAb3$^{[GluN1]}$-treated mice.** (A, B) Grip strength in female mice. Human IgG served as controls. There was no difference of mean forepaw (A) or mean 4-paw (B) grip strength in female mice. (C, D) Grip strength in male mice. There was no difference of mean forepaw (C) or mean 4-paw (D) grip strength in male mice. Above statistics were based on Mann-Whitney test.

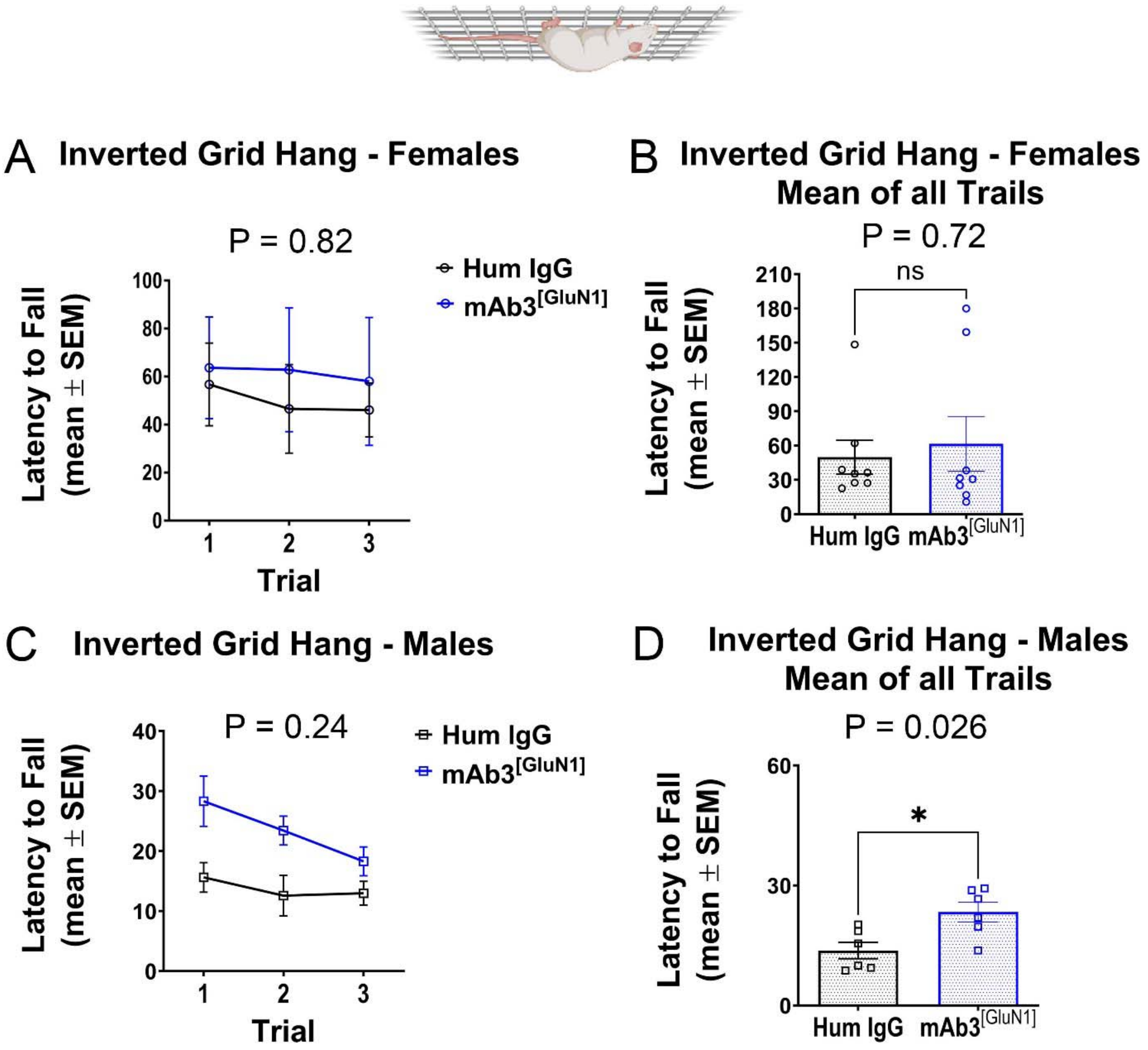

**Figure 6-figure supplementary 4: No impaired muscle strength and coordination in mAb3$^{[GluN1]}$-treated mice.** (A, B) Inverted grid hang of female mice. Human IgG served as controls. There were no differences of latency to fall in female mice. (C, D) Inverted grid hang of male mice. mAb3$^{[GluN1]}$-treated male mice took significantly longer to fall (B) compared to the control group, suggesting they exhibited better muscle coordination than controls. Above statistics were based on Mann-Whitney test.

**Supplementary Video 1: Represented balance beam performance of Human IgG treated female in 0.25x speed (Trail 4).**

**Supplementary Video 2: Represented balance beam performance of mAb3$^{[GluN1]}$-treated female in 0.25x speed (Trail 4).**

**Supplementary Video 3: Represented balance beam performance of Human IgG treated male in 0.25x speed (Trail 4).**

**Supplementary Video 4: Represented balance beam performance of mAb3$^{\text{[GluN1]}}$-treated male in 0.25x speed (Trail 4).**

**Supplementary Video 5: Represented facing up pole performance of Human IgG treated female in 0.5x speed (Trail 2).**

**Supplementary Video 6: Represented facing up pole performance of mAb3$^{\text{[GluN1]}}$-treated female in 0.5x speed (Trail 2).**

**Supplementary Video 7: Represented facing up pole performance of Human IgG treated male in 0.5x speed (Trail 3).**

**Supplementary Video 8: Represented facing up pole performance of mAb3$^{\text{[GluN1]}}$-treated male in 0.5x speed (Trail 3).**

**Table 1, Summary of morphological alterations in S1 callosal axons for mAb3$^{\text{[GluN1]}}$-treated mice.**

| Treatment | Gender | Branch Diameter | Branch Numbers | Branch Levels | Branch Angle | Branch ORIEN | Total Branch Length | Terminal Field Area |
|---|---|---|---|---|---|---|---|---|
| mAb3$^{\text{[GluN1]}}$ | **Female** | – | ↓ | – | – | – | ↓ | – |
| mAb3$^{\text{[GluN1]}}$ | **Male** | ↓ | | | | ←→ | | ↓ |

**−: No Change; ↓: Reduced; ↑: Increased; ←→: Opposite Direction**

**Table 2, Summary of impaired fine movements in mAb3$^{\text{[GluN1]}}$-treated mice.** Locomotor activity, muscle strength, and muscle coordination served as controls for baseline movement activity.

| Treatment | Gender | Locomotor Activity | Muscle Strength | Muscle Coordination | Nest Building | Balance Check | Latency of Facing Up Pole |
|---|---|---|---|---|---|---|---|
| mAb3$^{\text{[GluN1]}}$ | **Female** | – | – | – | – | ↓ | ↓ |
| mAb3$^{\text{[GluN1]}}$ | **Male** | – | – | – | ✖ | – | |

**−: No Change; ↑: Increased; X: Impaired**

A
CSF
B cell
Single cell Sorting
Mature B cells
mRNA extraction
cDNA
PCR: V(D)J
AAAA
Sequencing
Cloning & Antibody purification
H
L
AACATGGACGCC
HEK293
B
Negative Control
anti-NMDAR Encephalitis
260
160
125
90
Input
IgG
CSF
CSF
mAb #1
mAb #2
mAb #3
mAb #4
Anti-GluN1
Negative Control Patient CSF
anti-NMDAR Encephalitis CSF
C
D
mAb1
mAb3
E
F
CC
Ctx
OB
Hi
MB
CP
TH
CB
P
Med
G
EMX1
Cre
Rosa26
tdtomato
Reporter expression
H
EMX1^cre/+;Grin1^wt/wt;R26^tdT
I
EMX1^cre/+;Grin1^fl/fl;R26^tdT
mAb
R26^tdT
DAPI
mAb1
mAb3
J
Olfactory bulb
Cortex
Corpus callosum
Hippocampus
Cerebellum

A
Main subtypes of NMDA receptor in the cortex
GluN2A containing-
NMDA receptor
GluN1
GluN2A
GluN2A
GluN1
GluN2B containing-
NMDA receptor
GluN1
GluN2B
GluN2B
GluN1
B
GluN2A
GluN2A
GluN2B
GluN2B
Bi
EMX1cre/+;Grin1wt/wt;R26tdT
R26tdT
mAb
Dapi/mAb/R26tdT
mAb1
mAb3
Bii
EMX1cre/+;Grin1fl/fl;R26tdT
R26tdT
mAb
Dapi/mAb/R26tdT
mAb1
mAb3
C
Fluo. intensity per cell
40
30
20
10
0
*
mAb1
D
EMX1cre/+;Grin1wt/wt;R26tdT
EMX1cre/+;Grin1fl/fl;R26tdT
Overall Fluo. intensity
80
60
40
20
0
****
mAb1
E
EMX1cre/+;Grin1wt/wt;R26tdT
EMX1cre/+;Grin1fl/fl;R26tdT
Fluo. intensity per cell
80
60
40
20
0
****
mAb3
F
GluN2A
GluN2A
GluN1
GluN2B
GluN2B
GluN1
Fi
Grin2afl/fl
mAb
Dapi/mAb
mAb1
mAb3
Fii
EMX1cre/+;Grin2afl/fl
mAb
Dapi/mAb
mAb1
mAb3
G
Grin2afl/fl
EMX1cre/+;Grin2afl/fl
Norm. overall Fluo. intensity
100
80
60
40
20
0
****
mAb1
H
Grin2afl/fl
EMX1cre/+;Grin2afl/fl
Overall Fluo. intensity
20
15
10
5
0
ns
mAb3
I
GluN1
GluN2A
GluN2A
GluN1
GluN2B
GluN2B
Ii
EMX1cre/+;Grin2bwt/wt;R26tdT
R26tdT
mAb
Dapi/mAb/R26tdT
mAb1
mAb3
Iii
EMX1cre/+;Grin2bfl/fl;R26tdT
R26tdT
mAb
Dapi/mAb/R26tdT
mAb1
mAb3
J
EMX1cre/+;Grin2bwt/wt;R26tdT
EMX1cre/+;Grin2bfl/fl;R26tdT
Fluo. intensity per cell
50
40
30
20
10
0
ns
mAb1
K
EMX1cre/+;Grin2bwt/wt;R26tdT
EMX1cre/+;Grin2bfl/fl;R26tdT
Fluo. intensity per cell
80
60
40
20
0
ns
mAb3

A
E15.5
EGFP
Hum IgG
VS
mAb3[GluN1]
E14
E16
E18
P0
P2
P4
P6
P8
P10
P12
P14
B
S1
P14
S1
S2
Hum IgG
B'
S1
S2
B''
S1 cell bodies
S1
S2
C
S1
P14
S1
S2
mAb3[GluN1]
C'
S1
S2
C''
S1 cell bodies
S1
S2
D
Norm. Fluo. density in S1
****
0
5
10
15
Hum IgG
mAb3[GluN1]
E
EPHB2
S1
S1
F
EPHB2/Dapi
Contra S1
Injection S1
Hum IgG
mAb3[GluN1]
G
Injection/Contra S1 Fluo. Ratio
****
0.0
0.5
1.0
1.5
2.0
Hum IgG
mAb3[GluN1]

A
Female P120
Male P120
Hum IgG
mAb3[GluN1]
S1
S2
Y
Z
X
Axon Branch Points
Branch Terminal Points
Axon Branches
Diameter
Branch Length
Axon Branch Level
Level 1
Level 2
Level 3
Level 4
B
Female
Male
Norm. Fluo. density in S1
ns
Hum IgG
mAb3[GluN1]
150
100
50
0
C
Female
Male
Hum IgG
mAb3[GluN1]
D
Sholl Radius from start point of axon collateral
Sholl Distribution - Female
Sholl Distribution - Male
Sholl Axon Intersections (mean ± SEM)
Distance from start point (µm)
P < 0.0001
P = 0.45
E
Axon Branch Points Females
Branch Terminal Points Females
Total Branch Length Females
Axon Branch Diameter Females
Branch Resistance Females
Axon Branch Level Females
Axon Branch Points (mean ± SEM)
Branch Terminal Points (mean ± SEM)
Total Branch Length (mean ± SEM)
Axon Branch Diameter (mean ± SEM)
Mean Branch Resistance (mean ± SEM)
Axon Branch Level (mean ± SEM)
*
*
**
ns
ns
ns
F
Axon Branch Points Males
Branch Terminal Points Males
Total Branch Length Males
Axon Branch Diameter Males
Branch Resistance Males
Axon Branch Level Males
***
***
**
**
***
**
Axon Branch Orientation Angle
Angle to cortical surface
X-axis
B1
B2
γ1
γ2
Branching towards to Cortical Surface:
0 < γ1 < 180
Branching away from Cortical Surface:
-180 < γ2 < 0
G
Orientation Angles Females
Mean Orientation Angles (Degree, mean ± SEM)
ns
H
Orientation Angles Males
**
Orientation Angle - Female
Median Axon Branch Length (µm)
90
45
135
0
-180/180
-45
-135
-90

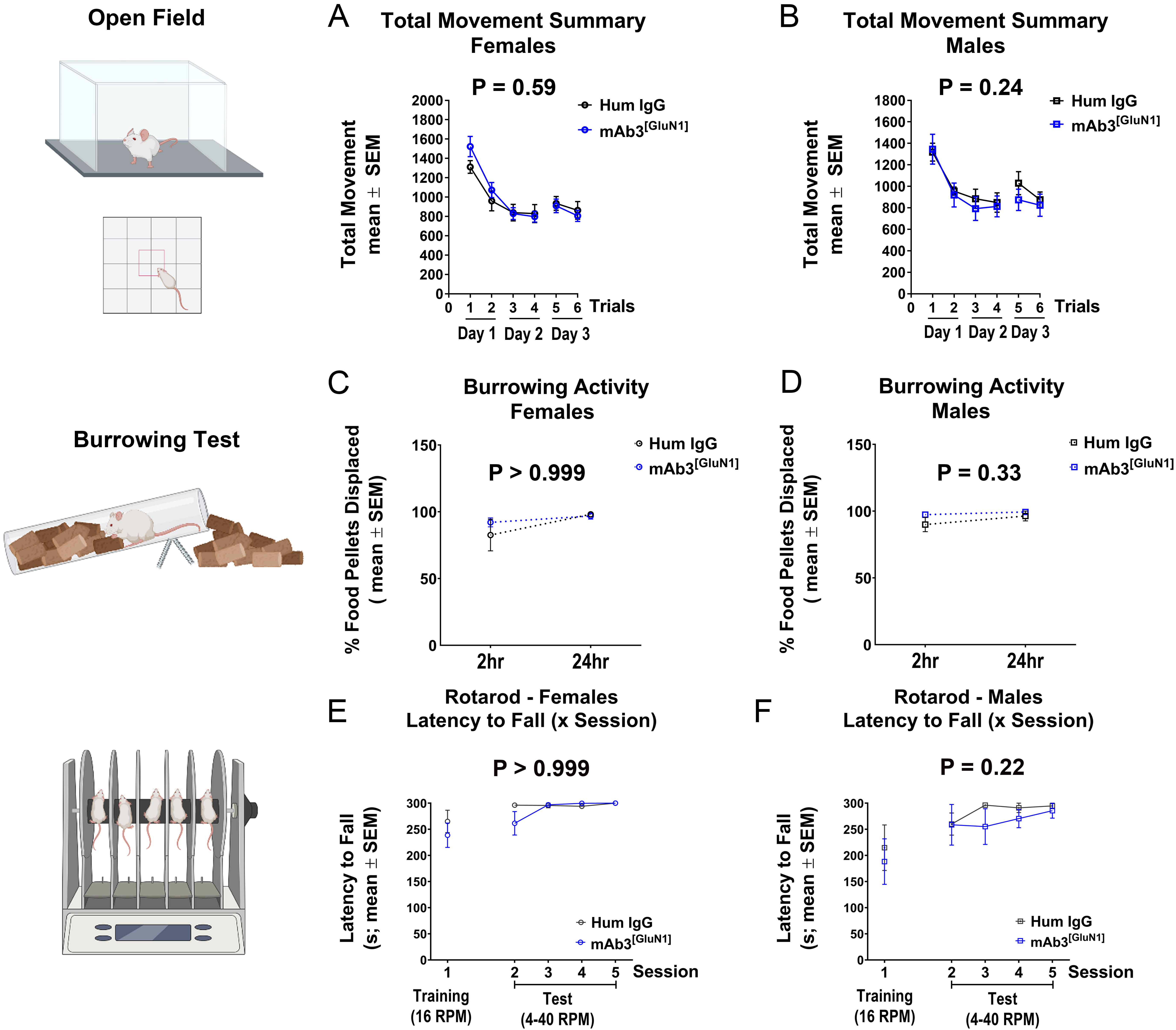

Open Field

Burrowing Test

A Total Movement Summary Females

B Total Movement Summary Males

C Burrowing Activity Females

D Burrowing Activity Males

E Rotarod - Females Latency to Fall (x Session)

F Rotarod - Males Latency to Fall (x Session)

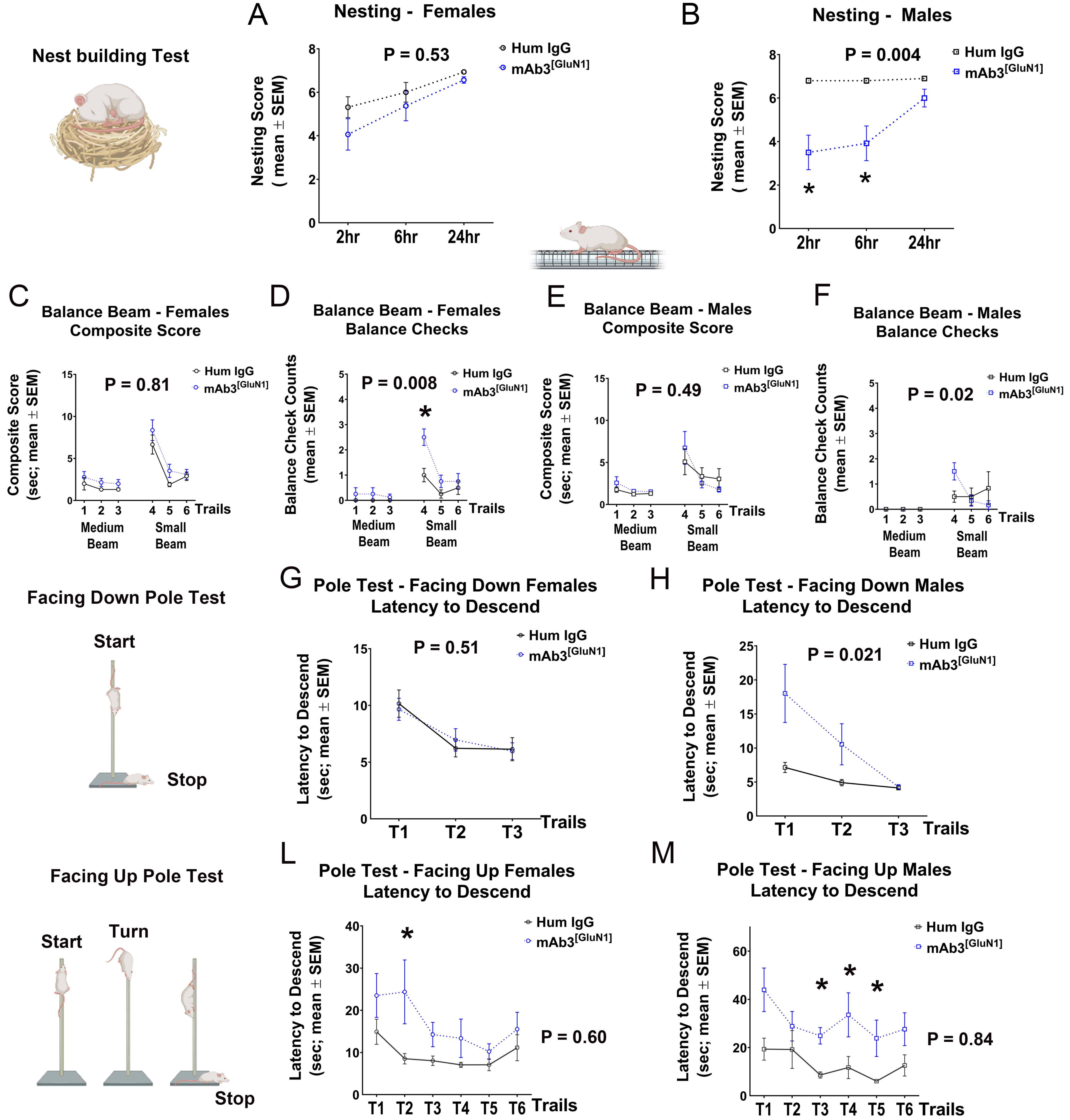
Nest building Test
A
Nesting - Females
P = 0.53
Hum IgG
mAb3[GluN1]
Nesting Score ( mean ± SEM)
0
2
4
6
8
2hr
6hr
24hr
B
Nesting - Males
P = 0.004
Hum IgG
mAb3[GluN1]
Nesting Score ( mean ± SEM)
*
*
0
2
4
6
8
2hr
6hr
24hr
C
Balance Beam - Females
Composite Score
P = 0.81
Hum IgG
mAb3[GluN1]
Composite Score (sec; mean ± SEM)
0
5
10
15
1 2 3 4 5 6 Trails
Medium Beam
Small Beam
D
Balance Beam - Females
Balance Checks
P = 0.008
Hum IgG
mAb3[GluN1]
*
Balance Check Counts (mean ± SEM)
0
1
2
3
4
5
1 2 3 4 5 6 Trails
Medium Beam
Small Beam
E
Balance Beam - Males
Composite Score
P = 0.49
Hum IgG
mAb3[GluN1]
Composite Score (sec; mean ± SEM)
0
5
10
15
1 2 3 4 5 6 Trails
Medium Beam
Small Beam
F
Balance Beam - Males
Balance Checks
P = 0.02
Hum IgG
mAb3[GluN1]
Balance Check Counts (mean ± SEM)
0
1
2
3
4
5
1 2 3 4 5 6 Trails
Medium Beam
Small Beam
Facing Down Pole Test
Start
Stop
G
Pole Test - Facing Down Females
Latency to Descend
P = 0.51
Hum IgG
mAb3[GluN1]
Latency to Descend (sec; mean ± SEM)
0
5
10
15
T1 T2 T3 Trails
H
Pole Test - Facing Down Males
Latency to Descend
P = 0.021
Hum IgG
mAb3[GluN1]
Latency to Descend (sec; mean ± SEM)
0
5
10
15
20
25
T1 T2 T3 Trails
Facing Up Pole Test
Start
Turn
Stop
L
Pole Test - Facing Up Females
Latency to Descend
*
Hum IgG
mAb3[GluN1]
P = 0.60
Latency to Descend (sec; mean ± SEM)
0
10
20
30
40
T1 T2 T3 T4 T5 T6 Trails
M
Pole Test - Facing Up Males
Latency to Descend
Hum IgG
mAb3[GluN1]
* * *
P = 0.84
Latency to Descend (sec; mean ± SEM)
0
20
40
60
T1 T2 T3 T4 T5 T6 Trails